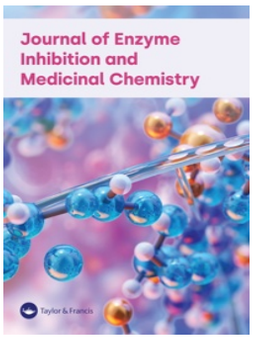

Journal of Enzyme Inhibition and Medicinal Chemistry

ISSN: 1475-6366 (Print) 1475-6374 (Online) Journal homepage: www.tandfonline.com/journals/ienz20

Imidazole-2-thione derivatives as new selective anticancer agents with anti-metastatic properties: synthesis and pharmacological evaluation

Božena Golcienė , Natalia Maciejewska, Anoop Kallingal , Birutė Sapijanskaitė-Banevič, Maryna Stasevych & Vytautas Mickevičius

To cite this article: Božena Golcienė , Natalia Maciejewska, Anoop Kallingal , Birutė Sapijanskaitė-Banevič, Maryna Stasevych & Vytautas Mickevičius (2026) Imidazole-2-thione derivatives as new selective anticancer agents with anti-metastatic properties: synthesis and pharmacological evaluation, Journal of Enzyme Inhibition and Medicinal Chemistry, 41:1, 2607820, DOI: 10.1080/14756366.2025.2607820

To link to this article: https://doi.org/10.1080/14756366.2025.2607820

JOURNAL OF ENZYME INHIBITION AND MEDICINAL CHEMISTRY
2025, VOL. 41, NO. 1, 2607820
https://doi.org/10.1080/14756366.2025.2607820

Taylor & Francis
Taylor & Francis Group

RESEARCH ARTICLE

OPEN ACCESS Check for updates

Imidazole-2-thione derivatives as new selective anticancer agents with anti-metastatic properties: synthesis and pharmacological evaluation

Božena Golcienė[a*], Natalia Maciejewska[b*], Anoop Kallingal[b], Birutė Sapijanskaitė-Banevič[a], Maryna Stasevych[c] and Vytautas Mickevičius[a]

[a]Department of Organic Chemistry, Kaunas University of Technology, Kaunas, Lithuania; [b]Department of Pharmaceutical Technology and Biochemistry, Faculty of Chemistry, Gdansk University of Technology, Gdansk, Poland; [c]Department of Technology of Biologically Active Substances, Pharmacy and Biotechnology, Lviv Polytechnic National University, Lviv, Ukraine

ABSTRACT

Imidazole scaffolds are attractive in drug design for bioactivity and synthetic accessibility. We developed S-substituted imidazole-2-thione derivatives, focusing on compound **24**, which showed potent cytotoxicity against lung, cervical, and colorectal cancer cells with submicromolar IC_{50} and selectivity over fibroblasts. Mechanistic analyses revealed G1 arrest, caspase-dependent apoptosis, and p-γH2AX accumulation. Importantly, compound **24** strongly inhibited A-549 cell migration and invasion in both 2D and 3D assays, correlating with downregulation of MMP-2, MMP-9, and hTERT. In vitro enzyme assays further confirmed that compound **24** directly inhibits MMP-9 activity. In vivo, **24** suppressed tumour growth and vasculotropic spread in the CAM model without detectable toxicity. Docking and dynamics simulations confirmed stable binding to MMP-2 and MMP-9 active sites. These results identify compound **24** as a promising anticancer agent with both cytotoxic and anti-metastatic properties, supporting its further preclinical investigation.

ARTICLE HISTORY
Received 3 October 2025
Revised 4 December 2025
Accepted 12 December 2025

KEYWORDS
Imidazole-2-thione; anticancer; anti-metastatic; lung cancer; MMPs

Introduction

Metastasis remains the primary cause of cancer mortality, accounting for roughly 90% of cancer-related death.[1] Aggressive malignancies often disseminate early and develop resistance to treatment, underscoring the need for therapies that can control both tumour growth and metastatic spread.[2] Traditional chemotherapy and targeted drugs typically focus on killing proliferating tumour cells but do not adequately address the complex, multi-step process of metastasis.[3,4] Often, surviving cancer cells can adapt under treatment pressure, becoming more invasive or metastatic and rendering single-target therapies ineffective.[5] One strategy to manage metastatic disease is to combine cytotoxic agents with specific anti-metastatic therapies (e.g., adding matrix metalloproteinases (MMP) or integrin inhibitors to chemotherapy).[6,7] However, combination regimens can be complex and poorly tolerated.[8,9] An attractive alternative is the development of multi-targeted anticancer agents – single compounds capable of exerting both cytotoxic and anti-metastatic effects. Such agents could simultaneously debulk the primary tumour and inhibit the dissemination of cancer cells, potentially improving outcomes in hard-to-treat tumours.

Imidazole-containing heterocycles are promising in this context, as they are well-established privileged scaffolds in medicinal chemistry.[10–12] The imidazole ring is present in numerous pharmacologically active compounds and approved drugs, including the alkylating prodrug dacarbazine, the multifunctional alkylating agent bendamustine, the tyrosine-kinase inhibitor ponatinib, and the DNA-methylating agent temozolomide (Scheme 1(a)).[13–15] In particular, imidazole-2-thione (an imidazole with a thione sulphur at

CONTACT Natalia Maciejewska natalia.maciejewska@pg.edu.pl Department of Pharmaceutical Technology and Biochemistry, Faculty of Chemistry, Gdansk University of Technology, Narutowicza St 11/12, 80-233 Gdansk, Poland
*These authors contributed equally.

Supplemental data for this article can be accessed online at https://doi.org/10.1080/14756366.2025.2607820.

the 2-position) has drawn interest due to its unique chemical properties. The 2-thione motif can engage in metal chelation and redox interactions, which may enable interference with multiple biological targets.[16] Notably, an imidazole-2-thione derivative PX-12 (1-methylpropyl 2-imidazolyl disulfide) has been developed as an irreversible thioredoxin-1 inhibitor and underwent clinical trials as a potential antitumor agent (Scheme 1(b)).[17,18] PX-12's ability to perturb the cellular redox environment and suppress tumour growth highlights the therapeutic potential of imidazole-2-thione scaffolds in oncology.[17,19]

Recent studies have provided evidence that appropriately functionalised imidazole-2-thiones can exhibit both cytotoxic and anti-metastatic activities. For example, various 2-oxo- and 2-thioxo-imidazole derivatives were shown to inhibit colony formation of melanoma and triple-negative breast cancer cells, as well as to restrict the growth of tumour spheroids – models representative of 3D tumour structure (Scheme 1(b)).[20–23] In our prior work, Golcienė *et al.* reported a series of 4-acetylphenylamine-substituted imidazole derivatives with promising anticancer effects (Scheme 1(b)).[24] Several compounds in that series not only displayed selective cytotoxicity towards cancer cells but also suppressed the expansion of 3D tumour spheroids in breast, prostate, and brain cancer models.[24] These findings suggested that the imidazole-2-thione core could be leveraged to yield dual-function agents that both kill tumour cells and impair their metastatic potential.

The structural motifs illustrated in Scheme 1 guided the design of the present imidazole-2-thione series. The clinically used imidazole-containing agents (Scheme 1(a)) and the previously reported 2-oxo/2-thioxo analogues with anti-proliferative and anti-spheroid activity (Scheme 1(b)) highlight two features that informed our scaffold selection: (i) aryl substituents on the heterocycle strongly influence biological activity through modulation of lipophilicity, electronic density, and protein-binding orientation, and (ii) variation at the sulphur-containing C2 position can tune interactions with zinc-dependent enzymes and redox-sensitive cellular targets. On this basis, we constructed a panel of S-substituted imidazole-2-thione derivatives bearing systematically altered aryl ring patterns (H, halogen, and electron-withdrawing groups) and distinct S-alkyl or S-acyl fragments. These modifications were chosen to explore how steric bulk, electron-withdrawing capacity, and thione-driven metal-binding

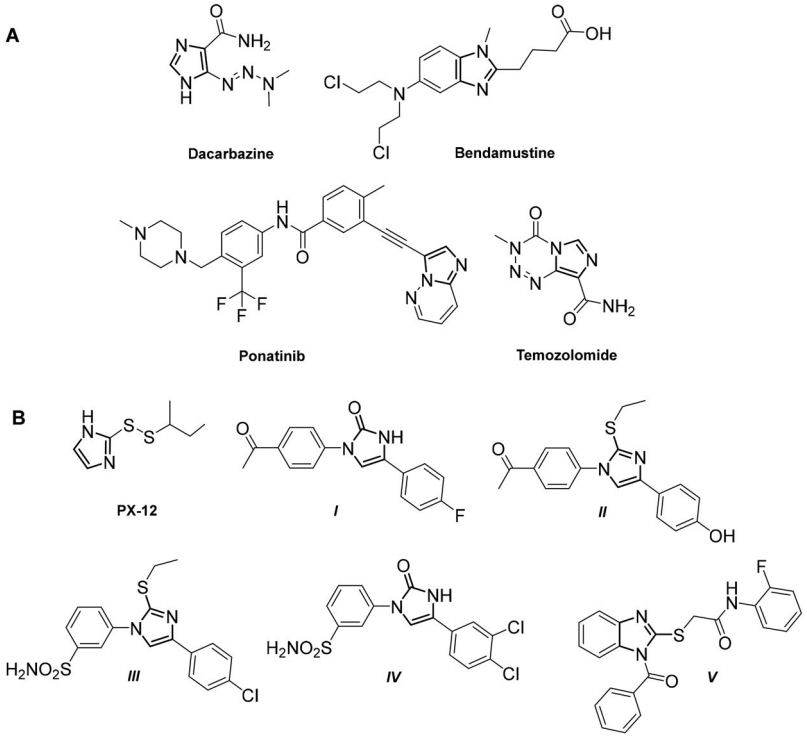

Scheme 1. Overview of imidazole-based anticancer scaffolds relevant to the design of new imidazole-2-thione derivatives. (a). Examples of clinically used imidazole scaffold-containing agent. (b) PX-12 and representative 2-oxo/2-thioxo imidazole derivatives (e.g. *I*–*V*, from refs. [20–24]) reported to inhibit colony formation and suppress 3D tumour spheroid growth, supporting the rationale for new imidazole-2-thione candidates.

potential—features visible in the reference structures—shape cytotoxic, anti-migratory, and anti-invasive behaviour. In this way, the structural elements in Scheme 1 provided a direct chemical rationale for assembling the new library. To build upon our earlier work on imidazole scaffolds, the present study deliberately extends beyond cytotoxic profiling into two mechanistic domains not previously explored in our series: direct engagement of matrix metalloproteinases and *in vivo* inhibition of metastatic behaviour. While our prior derivatives demonstrated selective cytotoxicity and suppression of spheroid expansion, they were not evaluated for MMP modulation nor tested in embryonic models of dissemination. Given the integral role of MMP-2 and MMP-9 in extracellular matrix degradation and metastatic spread, the new S-substituted imidazole-2-thione library was designed to probe their zinc-dependent active sites through the thione moiety and sterically tuned aryl substituents. This broadened biological framework—linking rational structural design with MMP targeting and *in vivo* anti-metastatic validation—situates the present series as an advancement over earlier imidazole analogues and clarifies the rationale for the new chemical panel.

Materials and methods

Chemistry

General procedures for chemistry

Reagents and solvents were purchased from Sigma-Aldrich (St. Louis, MO, USA) and used without further purification. The reaction course and purity of the synthesised compounds were monitored by TLC using aluminium plates pre-coated with Silica gel with F_{254} nm (Merck KGaA, Darmstadt, Germany). Melting points were determined with a *B-540* melting point analyser (Büchi Corporation, New Castle, DE, USA) and were uncorrected. IR spectra (ν, cm^{-1}) were recorded on a Vertex70 FT–IR spectrometer (Bruker, USA) using KBr pellets. NMR spectra were recorded on a Brucker Avance III (400, 101 MHz) spectrometer (Bruker BioSpin AG, Fällanden, Switzerland). Chemical shifts were reported in (δ) ppm relative to tetramethylsilane (TMS), with the residual solvent as internal reference (DMSO-d_6, $\delta = 2.50$ ppm for ^{1}H NMR and $\delta = 39.52$ ppm for ^{13}C NMR). Data are reported as follows: chemical shift, multiplicity, integration, coupling constant [Hz], and assignment. Elemental analyses (C, H, N) were conducted using the Elemental Analyser CE-440 (ExeterAnalytical, Inc., Chelmsford, MA, USA); their results were found to be in good agreement(±0.3%) with the calculated values.

Synthetic procedures

Compounds **1 – 5** were synthesised according to the procedure reported in.[24] The ^{1}H and ^{13}C-NMR and HRMS spectra agreed with that given in the study (Figures S1–S51 in Supplementary File).

General procedure A: for the synthesis of imidazoles 6 – 10

To a solution of the corresponding imidazolethione**1 – 5** (2 mmol) in methanol (70 ml) anhydrous K_2CO_3 (2 mmol, 0.27 g) and methyl bromoacetate (4 mmol, 0.61 g, 0.37 ml) were added, and the reaction mixture was heated at reflux for 2 h. Afterward, methanol was evaporated under reduced pressure, and the residue was poured with water. The resulting solid was filtered off, washed with water, and dried.

Methyl 2-((1–(4-acetylphenyl)-4-phenyl-1H-imidazol-2-yl)thio)acetate (6). Synthesis according to the General procedure **A**, using **1** (0.59 g, 2 mmol). White solid (0.64 g, 88% yield); m.p. 148–149 °C (propan-2-ol); IR (KBr) (ν, cm^{-1}): 1595 (C = N); 1667; 1738 (2 C = O); ^{1}H NMR (400 MHz, DMSO-d_6) δ (ppm): 2.65 (s, 3H, CH_3), 3.65 (s, 3H, OCH_3), 4.09 (s, 2H, CH_2), 7.25 (t, 1H, $J = 7.4$ Hz, H_{Ar}), 7.40 (t, 2H, $J = 7.2$ Hz, H_{Ar}), 7.71 (d, 2H, $J = 8.4$ Hz, H_{Ar}), 7.81 (d, 2H, $J = 7.8$ Hz, H_{Ar}), 8.09–8.19 (m, 3H, CH, H_{Ar}); ^{13}C NMR (101 MHz, DMSO-d_6) δ (ppm): 27.4 (CH_3), 35.4 (CH_2), 52.8 (OCH_3), 119.3 (CH), 124.8, 125.2, 127.4, 129.1, 130.2, 133.7, 136.7, 140.6 (C–S), 141.3 (CN), 141.9 (C_{Ar}), 169.6 (CH_2C=O), 197.5 (C = O); Anal. Calcd. for $C_{20}H_{18}N_2O_3S$: C 65.56; H 4.95; N 7.65%; Found: C 65.86; H 5.09; N 7.83%.

Methyl 2-((1–(4-acetylphenyl)-4–(4-chlorophenyl)-1H-imidazol-2-yl)thio)acetate (7). Synthesis according to the General procedure **A**, using **2** (0.67 g, 2 mmol). White solid (0.78 g, yield 98%); m.p. 161–162 °C

(propan-2-ol); IR (KBr) (v, cm^{-1}): 1596 (C=N); 1660; 1739 (2C=O); ^{1}H NMR (400 MHz, DMSO-d_6) δ (ppm): 2.65 (s, 3H, CH_3), 3.64 (s, 3H, OCH_3), 3.96 (s, 2H, CH_2), 7.46 (d, 2H, J=6.8 Hz, H_{Ar}), 7.70 (d, 2H, J=6.8 Hz, H_{Ar}), 7.81 (d, 2H, J=8.6 Hz, H_{Ar}), 8.13 (s, 2H, H_{Ar}), 8.15 (s, 1H, CH); ^{13}C NMR (101 MHz, DMSO-d_6) δ (ppm): 27.4 (CH_3), 35.3 (CH_2), 51.9 (OCH_3), 119.4 (CH), 125.3, 126.5, 129.1, 130.1, 131.6, 132.8, 136.3, 140.6 (C–S), 140.7 (CN), 143.0 (C_{Ar}), 170.2 (CH_2C=O), 197.6 (C=O); Anal. Calcd. for $C_{20}H_{17}ClN_2O_3S$: C 59.92; H 4.27; N 6.99%; Found: C 60.26; H 4.44; N 6.95%.

Methyl 2-((1–(4-acetylphenyl)-4–(4-hydroxyphenyl)-1H-imidazol-2-yl)thio)acetate (8). Synthesis according to the General procedure **A**, using **3** (0.62 g, 2 mmol). Light yellow solid (0.57 g, yield 74%); m.p. 174–175 °C (propan-2-ol); IR (KBr) (v, cm^{-1}): 1592 (C=N); 1663; 1733 (2C=O); 3071 (OH); ^{1}H NMR (400 MHz, DMSO-d_6) δ (ppm): 2.64 (s, 3H, CH_3), 3.64 (s, 3H, OCH_3), 4.06 (s, 2H, CH_2), 6.79 (d, 2H, J=8.2 Hz, H_{Ar}), 7.61 (d, 2H, J=8.2 Hz, H_{Ar}), 7.68 (d, 2H, J=8.2 Hz, H_{Ar}), 7.90 (s, 1H, CH), 8.14 (d, 2H, J=8.3 Hz, H_{Ar}), 9.45 (s, 1H, OH); ^{13}C NMR (101 MHz, DMSO-d_6) δ (ppm): 27.4 (CH_3), 35.4 (CH_2), 52.8 (OCH_3), 115.8 (CH), 117.7, 124.9, 125.1, 126.2, 130.1, 136.5, 140.6 (C–S), 140.7, 142.4 (CN), 157.1 (C_{Ar}), 169.7 (CH_2C=O), 197.5 (C=O); Anal. Calcd. for $C_{20}H_{18}N_2O_4S$: C 62.81; H 4.74; N 7.33%; Found: C 62.74; H 5.04; N 7.20%.

Methyl 2-((1–(4-acetylphenyl)-4–(4-fluorophenyl)-1H-imidazol-2-yl)thio)acetate (9). Synthesis according to the General procedure **A**, using **4** (0.62 g, 2 mmol). White solid (0.69 g, yield 90%); m.p. 172–173 °C (propan-2-ol); IR (KBr) (v, cm^{-1}): 1599 (C=N); 1683; 1739 (2C=O);^{1}H NMR (400 MHz, DMSO-d_6) δ (ppm): 2.28 (s, 3H, CH_3), 3.65 (s, 3H, OCH_3), 4.19 (s, 2H, CH_2), 7.23 (t, 2H, J=8.9 Hz, H_{Ar}), 7.70 (d, 2H, J=8.6 Hz, H_{Ar}), 7.81–7.84 (m, 2H, H_{Ar}), 8.09 (s, 1H, CH), 8.15 (d, 2H, J=8.6 Hz, H_{Ar}); ^{13}C NMR (101 MHz, DMSO-d_6) δ (ppm): 27.4 (CH_3), 35.3 (CH_2), 52.8 (OCH_3), 115.9 (d, J=21.5 Hz C-3,5), 119.2, 125.2, 126.7 (d, J=8.1, Hz C-2,6), 130.3 (d, J=3.1, Hz C-1), 130.3, 136.7, 140.5 (C–S), 141.0 (CN), 141.4 (C_{Ar}), 161.8 (d, J=243, Hz C–F), 169.6 (CH_2C=O), 197.5 (C=O); Anal. Calcd. for $C_{20}H_{17}FN_2O_3S$: C 62.49; H 4.46; N 7.29%; Found: C 62.16; H 4.59; N 7.31%.

Methyl 2-((1–(4-acetylphenyl)-4–(4-nitrophenyl)-1H-imidazol-2-yl)thio)acetate (10). Synthesis according to the General procedure **A**, using **5** (0.68 g, 2 mmol). Dark red solid (0.76 g, yield 92%); m.p. 185–186 °C (propan-2-ol); IR (KBr) (v, cm^{-1}): 1592 (C=N); 1676; 1746 (2C=O); ^{1}H NMR (400 MHz, DMSO-d_6) δ (ppm): 2.65 (s, 3H, CH_3), 3.66 (s, 3H, OCH_3), 4.13 (s, 2H, CH_2), 7.73 (d, 2H, J=8.2 Hz, H_{Ar}), 8.03 (d, 2H, J=8.5 Hz, H_{Ar}), 8.17 (d, 2H, J=8.3 Hz, H_{Ar}), 8.28 (d, 2H, J=8.5 Hz, H_{Ar}), 8.43 (s, 1H, CH); ^{13}C NMR (101 MHz, DMSO-d_6) δ (ppm): 27.4 (CH_3), 35.3 (CH_2), 52.9 (OCH_3), 122.5 (CH), 124.7, 125.3, 125.4, 130.2, 137.0, 139.8, 140.2, 140.3 (C–S), 142.9 (CN), 146.3 (C_{Ar}), 169.6 (CH_2C=O), 197.5 (C=O);Anal. Calcd. for $C_{20}H_{17}N_3O_5S$: C 58.39; H 4.16; N 10.21%; Found: C 58.72; H 4.28; N 10.49%.

General procedure B: for the synthesis of imidazoles 11 – 15

A mixture of the corresponding methyl acetate **6 – 10** (2 mmol) was heated at reflux in diluted hydrochloric acid (10 ml HCl/10 ml H_2O) for 1 h. Then the reaction mixture was cooled, the formed crystalline filtered off, and dried.

2-((1–(4-Acetylphenyl)-4-phenyl-1H-imidazol-2-yl)thio)acetic acid (11). Synthesis according to the General procedure **B B**, using **6** (0.73 g, 2 mmol). White solid (0.68 g, yield 97%); m.p. 153–154 °C (water); IR (KBr) (v, cm^{-1}): 1598 (C=N); 1676; 1725 (2C=O); 3113 (OH); ^{1}H NMR (400 MHz, DMSO-d_6) δ (ppm): 2.65 (s, 3H, CH_3), 4.05 (s, 2H, CH_2), 7.26 (t, 1H, J=7.4 Hz, H_{Ar}), 7.40 (t, 2H, J=7.7 Hz, H_{Ar}), 7.71 (d, 2H, J=8.6 Hz, H_{Ar}), 7.83 (d, 2H, J=7.1 Hz, H_{Ar}), 8.12 (s, 1H, CH), 8.15 (d, 2H, J=8.6 Hz, H_{Ar}), 12.87 (br. s, 1H, OH); ^{13}C NMR (101 MHz, DMSO-d_6) δ (ppm): 27.4 (CH_3), 35.8 (CH_2), 119.2 (CH), 124.8, 124.9, 125.2, 127.5, 129.1, 130.2, 133.7, 136.7, 140.6 (C–S), 141.8 (CN), 141.8 (C_{Ar}), 170.3 (COOH), 197.4 (C=O); Anal. Calcd. for $C_{19}H_{16}N_2O_3S$: C 64.76; H 4.58; N 7.95%; Found: C 64.38; H 4.66; N 7.85%.

2-((1–(4-Acetylphenyl)-4–(4-chlorophenyl)-1H-imidazol-2-yl)thio)acetic acid (12). Synthesis according to the General procedure **B**, using **7** (0.80 g, 2 mmol). Light yellow solid (0.75 g, yield 97%); m.p. 151–152 °C (methanol); IR (KBr) (v, cm^{-1}): 1599 (C=N); 1663; 1732 (2C=O); 3114 (OH); ^{1}H NMR (400 MHz, DMSO-d_6) δ (ppm): 2.65 (s, 3H, CH_3), 4.07 (s, 2H, CH_2), 7.47 (d, 2H, J=8.3 Hz, H_{Ar}), 7.71 (d, 2H, J=8.2 Hz, H_{Ar}), 7.85 (d, 2H, J=8.3 Hz, H_{Ar}), 8.15 (d, 2H, J=8.2 Hz, H_{Ar}), 8.20 (s, 1H, CH); ^{13}C NMR (101 MHz, DMSO-d_6) δ (ppm): 27.4

(CH_3), 35.4 (CH_2), 119.8 (CH), 125.4, 126.6, 129.1, 130.2, 131.9, 132.2, 136.8, 140.3 (C–S), 140.4 (CN), 142.1 (C_{Ar}), 170.2 (COOH), 197.5 (C=O); Anal. Calcd. for $C_{19}H_{15}ClN_2O_3S$: C 58.99; H 3.91; N 7.24%; Found: C 58.75; H 4.09; N 7.04%.

2-((1–(4-Acetylphenyl)-4–(4-hydroxyphenyl)-1H-imidazol-2-yl)thio)acetic acid (13). Synthesis according to the General procedure **B**, using **8** (0.76 g, 2 mmol). Beige solid (0.52 g, yield 74%); m.p. 106–107 °C (propan-2-ol); IR (KBr) (v, cm^{-1}): 1597 (C=N); 1683; 1712 (2C=O); 3056; 3106 (2OH); ^{1}H NMR (400 MHz, DMSO-d_6) δ (ppm): 2.65 (s, 3H, CH_3), 4.07 (s, 2H, CH_2), 7.25 (t, 2H, J=8.0 Hz, H_{Ar}), 7.71 (d, 2H, J=8.6 Hz, H_{Ar}), 7.81–7.91 (m, 2H, H_{Ar}), 8.15 (s, 2H, H_{Ar}) 8.17 (s, 1H, CH), 12.42 (br. s, 1H, OH); ^{13}C NMR (101 MHz, DMSO-d_6) δ (ppm): 27.4 (CH_3), 35.9 (CH_2), 115.9 (CH), 116.1, 119.2, 125.4, 126.9, 126.9, 130.2, 136.8, 140.4 (C–S), 141.8 (CN), 160.7 (C_{Ar}), 170.2 (COOH), 197.5 (C=O);Anal. Calcd. for $C_{19}H_{16}N_2O_4S$: C 61.94; H 4.38; N 7.60%; Found: C 61.68; H 4.18; N 7.36%.

2-((1–(4-Acetylphenyl)-4–(4-fluorophenyl)-1H-imidazol-2-yl)thio)acetic acid (14). Synthesis according to the General procedure **B**, using **9** (0.77 g, 2 mmol). White solid (0.68 g, yield 93%); m.p. 167–168 °C (propan-2-ol); IR (KBr) (v, cm^{-1}): 1591 (C=N); 1684; 1732 (2C=O); 3106 (OH); ^{1}H NMR (400 MHz, DMSO-d_6) δ (ppm): 2.65 (s, 3H, CH_3), 4.14–4.22 (m, 2H, CH_2), 7.29 (t, 2H, J=8.5 Hz, H_{Ar}), 7.75 (d, 2H, J=8.4 Hz, H_{Ar}), 7.90–7.98 (m, 2H, H_{Ar}), 8.17 (d, 2H, J=8.3 Hz, H_{Ar}) 8.22–8.30 (m, 1H, CH), 11.00 (br. s, 1H, OH); ^{13}C NMR (101 MHz, DMSO-d_6) δ (ppm): 27.4 (CH_3), 36.5 (CH_2), 116.2 (d, J=21.8 Hz, C-3,5), 119.8, 125.9, 125.2, 127.4 (d, J=8.1 Hz, C-2,6), 130.1, 137.3, 139.9 (C–S), 140.1 (CN), 141.9 (C_{Ar}), 162.2 (d, J=245.2 Hz, C–F), 170.0 (COOH), 197.6 (C=O); Anal. Calcd. for $C_{19}H_{15}FN_2O_3S$: C 61.61; H 4.08; N 7.56%; Found: C 61.49; H 4.18; N 7.32%.

2-((1–(4-Acetylphenyl)-4–(4-nitrophenyl)-1H-imidazol-2-yl)thio)acetic acid (15). Synthesis according to the General procedure **B**, using **10** (0.82 g, 2 mmol). Dark orange solid (0.58 g, yield 73%); m.p. 205–206 °C (propan-2-ol); IR (KBr) (v, cm^{-1}): 1599 (C=N); 1683; 1718 (2C=O); 3120 (OH); ^{1}H NMR (400 MHz, DMSO-d_6) δ (ppm): 2.66 (s, 3H, CH_3), 4.09 (s, 2H, CH_2), 7.74 (d, 2H, J=8.3 Hz, H_{Ar}), 8.06 (d, 2H, J=8.7 Hz, H_{Ar}), 8.16 (d, 2H, J=8.4 Hz, H_{Ar}), 8.28 (d, 2H, J=8.7 Hz, H_{Ar}), 8.45 (s, 1H, CH), 12.17 (br. s, 1H, OH); ^{13}C NMR (101 MHz, DMSO-d_6) δ (ppm): 27.4 (CH_3), 35.7 (CH_2), 122.5 (CH), 124.7, 125.4, 125.4, 130.2, 137.0, 139.7, 140.2, 140.2 (C–S), 143.4 (CN), 146.3 (C_{Ar}), 170.1 (COOH), 197.6 (C=O); Anal. Calcd. for $C_{19}H_{15}N_3O_5S$: C 57.42; H 3.80; N 10.57%; Found: C 57.22; H 3.92; N 10.39%.

General procedure C: for the synthesis of imidazole derivatives 16 – 20

To a solution of the corresponding thioimidazole **1 – 5** (2 mmol) in methanol (70 ml) anhydrous K_2CO_3 (2 mmol, 0.27 g), and 1-chloropropan-2-one (4 mmol, 0.37 g, 0.32 ml) were added, and the reaction mixture was heated at reflux for 1 h. Afterward, the solvent was evaporated under reduced pressure, and the residue was poured with water. The resulting solid was filtered off, washed with water, and dried.

1-((1–(4-Acetylphenyl)-4-phenyl-1H-imidazol-2-yl)thio)propan-2-one (16). Synthesis according to the General procedure **C**, using **1** (0.59 g, 2 mmol). Light yellow solid (0.60 g, yield 86%); m.p. 102–103 °C (propan-2-ol); IR (KBr) (v, cm^{-1}): 1598 (C=N); 1670; 1711 (2C=O); ^{1}H NMR (400 MHz, DMSO-d_6) δ (ppm): 2.28 (s, 3H, CH_3), 2.65 (s, 3H, CH_3), 4.19 (s, 2H, CH_2), 7.25 (t, 1H, J=7.4 Hz, H_{Ar}), 7.39 (t, 2H, J=7.7 Hz, H_{Ar}), 7.71 (d, 2H, J=8.6 Hz, H_{Ar}), 7.80 (d, 2H, J=7.1 Hz, H_{Ar}), 8.10 (s, 1H, CH), 8.15 (t, 2H, J=8.6 Hz, H_{Ar}); ^{13}C NMR (101 MHz, DMSO-d_6) δ (ppm): 27.4 (CH_3), 29.3 (CH_2), 43.7 (CH_3), 119.2 (CH), 124.8, 125.2, 127.4, 129.1, 130.2, 133.7, 136.7, 140.6 (C–S), 141.7 (CN), 141.8 (C_{Ar}), 197.5 (C=O), 202.9 (CH_2C=O); Anal. Calcd. for $C_{20}H_{18}N_2O_2S$: C 68.55; H 5.18; N 7.99%; Found: C 68.22; H 5.35; N 7.96%.

1-((1–(4-Acetylphenyl)-4–(4-chlorophenyl)-1H-imidazol-2-yl)thio)propan-2-one (17). Synthesis according to the General procedure **C**, using **2** (0.67 g, 2 mmol). White solid (0.76 g, yield 99%); m.p. 124–123 °C (propan-2-ol); IR (KBr) (v, cm^{-1}): 1584 (C=N); 1683; 1725 (2C=O); ^{1}H NMR (400 MHz, DMSO-d_6) δ (ppm): 2.27 (s, 3H, CH_3), 2.65 (s, 3H, CH_3), 4.20 (s, 2H, CH_2), 7.46 (d, 2H, J=8.4 Hz, H_{Ar}), 7.71 (d, 2H, J=8.4 Hz, H_{Ar}), 7.81 (d, 2H, J=7.0 Hz, H_{Ar}), 8.12–8.16 (m, 3H, CH, H_{Ar}); ^{13}C NMR (101 MHz, DMSO-d_6) δ (ppm): 27.4 (CH_3), 29.3 (CH_2), 43.7 (CH_3), 119.7 (CH), 125.3, 126.45, 129.1, 130.2, 131.7, 132.7, 136.7, 140.5 (C–S), 140.7 (CN), 142.1 (C_{Ar}), 197.5 (C=O), 202.9 (CH_2C=O); Anal. Calcd. for $C_{20}H_{17}ClN_2O_2S$: C 62.41; H 4.45; N 7.28%; Found: C 62.06; H 4.59; N 7.02%.

1-((1–(4-Acetylphenyl)-4–(4-hydroxyphenyl)-1H-imidazol-2-yl)thio)propan-2-one (18). Synthesis according to the General procedure **C**, using **3** (0.62 g, 2 mmol). Yellow solid (0.51 g, yield 70%); m.p. 166–167 °C (propan-2-ol); IR (KBr) (ν, cm^{-1}): 1606 (C=N); 1673; 1698 (2C=O); 3099 (OH); ^{1}H NMR (400 MHz, DMSO-d_6) δ (ppm): 2.27 (s, 3H, CH_3), 2.64 (s, 3H, CH_3), 4.16 (s, 2H, CH_2), 6.78 (d, 2H, J=8.7 Hz, H_{Ar}), 7.60 (d, 2H, J=8.6 Hz, H_{Ar}), 7.69 (d, 2H, J=8.6 Hz, H_{Ar}), 7.88 (s, 1H, CH), 8.14 (d, 2H, J=8.6 Hz, H_{Ar}), 9.48 (s, 1H, OH); ^{13}C NMR (101 MHz, DMSO-d_6) δ (ppm): 27.3 (CH_3), 29.3 (CH_2), 43.7 (CH_3), 115.8 (CH), 117.3, 124.9, 125.1, 126.2, 130.1, 136.5, 140.8 (C–S), 141.0 (CN), 142.3, 157.1 (C_{Ar}), 197.5 (C=O), 203.0 (CH_2C=O);Anal. Calcd. for $C_{20}H_{18}N_2O_3S$: C 65.56; H 4.95; N 7.65%; Found: C 64.29; H 5.05; N 7.41%.

1-((1–(4-Acetylphenyl)-4–(4-fluorophenyl)-1H-imidazol-2-yl)thio)propan-2-one (19). Synthesis according to the General procedure **C**, using **4** (0.62 g, 2 mmol). Light beige solid (0.65 g, yield 89%); m.p. 167–168 °C (propan-2-ol); IR (KBr) (ν, cm^{-1}): 1560 (C=N); 1683; 1718 (2C=O); 3099 (OH); ^{1}H NMR (400 MHz, DMSO-d_6) δ (ppm): 2.28 (s, 3H, CH_3), 2.65 (s, 3H, CH_3), 4.19 (s, 2H, CH_2), 7.23 (t, 2H, J=8.9 Hz, H_{Ar}), 7.70 (d, 2H, J=8.6 Hz, H_{Ar}), 7.81–7.84 (m, 2H, H_{Ar}), 8.09 (s, 1H, CH), 8.15 (d, 2H, J=8.6 Hz, H_{Ar}); ^{13}C NMR (101 MHz, DMSO-d_6) δ (ppm): 27.4 (CH_3), 29.3 (CH_2), 43.7 (CH_3), 115.9 (d, J=21.5 Hz, C-3,5), 119.0, 125.2, 125.2, 126.7 (d, J=8.1 Hz, C-2,6), 130.2, 130.3 (d, J=2.9 Hz, C-1), 136.7, 140.6 (C–S), 140.9 (CN), 141.8 (C_{Ar}), 161.8 (d, J=243.3 Hz C–F), 197.5 (C=O), 202.9 (CH_2C=O); Anal. Calcd. for $C_{20}H_{17}FN_2O_2S$: C 65.20; H 4.65; N 7.60%; Found: C 65.13; H 4.85; N 7.40%.

1-((1–(4-Acetylphenyl)-4–(4-nitrophenyl)-1H-imidazol-2-yl)thio)propan-2-one (20). Synthesis according to the General procedure **C**, using **5** (0.68 g, 2 mmol). Dark red solid (0.71 g, yield 90%); m.p. 198–199 °C (propan-2-ol); IR (KBr) (ν, cm^{-1}): 1599 (C=N); 1682; 1710 (2C=O); ^{1}H NMR (400 MHz, DMSO-d_6) δ (ppm): 2.29 (s, 3H, CH_3), 2.65 (s, 3H, CH_3), 4.25 (s, 2H, CH_2), 7.73 (d, 2H, J=8.6 Hz, H_{Ar}), 8.03 (d, 2H, J=8.9 Hz, H_{Ar}), 8.16 (d, 2H, J=8.6 Hz, H_{Ar}), 8.27 (d, 2H, J=9.0 Hz, H_{Ar}), 8.41 (s, 1H, CH); ^{13}C NMR (101 MHz, DMSO-d_6) δ (ppm): 27.4 (CH_3), 29.4 (CH_2), 43.7 (CH_3), 122.4 (CH), 124.7, 125.3, 125.4, 130.2, 136.9, 139.7, 140.2, 140.3 (C–S), 143.4 (CN), 146.2 (C_{Ar}), 197.5 (C=O), 202.8 (CH_2C=O); Anal. Calcd. for $C_{20}H_{17}FN_2O_2S$: C 60.75; H 4.33; N 10.63%; Found: C 60.36; H 4.56; N 10.39%.

General procedure D: for the synthesis of imidazole derivatives 21 – 30

To a solution of the corresponding imidazolethione **1** or **2** (2 mmol) in methanol (70 ml) anhydrous K_2CO_3 (2 mmol, 0.27 g) and the corresponding bromoacetophenone (4 mmol) were added, and the reaction mixture was heated at reflux for 2 h. After completion of the reaction, methanol was evaporated under reduced pressure, and the residue was poured with water. The resulting solid was filtered off, washed with water, and dried.

2-((1–(4-Acetylphenyl)-4-phenyl-1H-imidazol-2-yl)thio)-1-phenylethan-1-one (21). Synthesis according to the General procedure **D**, using **1** (0.59 g, 2 mmol), and 4′-bromoacetophenone (0.80 g, 4 mmol). White solid (0.82 g, yield 99.5%); m.p. 137–138 °C (propan-2-ol); IR (KBr) (ν, cm^{-1}): 1606 (C=N); 1676 (2C=O); ^{1}H NMR (400 MHz, DMSO-d_6) δ (ppm): 2.64 (s, 3H, CH_3), 4.84 (s, 2H, CH_2), 7.20 (t, 1H, J=7.3 Hz, H_{Ar}), 7.30 (t, 2H, J=7.6 Hz, H_{Ar}), 7.55 (t, 2H, J=7.7 Hz, H_{Ar}), 7.65–7.71 (m, 5H, H_{Ar}), 8.03 (d, 2H, J=7.7 Hz, H_{Ar}), 8.09 (s, 1H, CH), 8.13 (d, 2H, J=7.3 Hz, H_{Ar}); ^{13}C NMR (101 MHz, DMSO-d_6) δ (ppm): 27.4 (CH_3), 40.8 (CH_2), 119.2 (CH), 124.8, 125.3, 127.3, 128.9, 128.9, 130.1, 133.7, 133.9, 136.3, 136.6, 140.7 (C–S), 141.5 (CN), 141.8 (C_{Ar}), 194.5 (CH_2C=O), 197.5 (C=O); Anal. Calcd. for $C_{25}H_{20}N_2O_2S$: C 72.79; H 4.89; N 6.79%; Found: C 72.42; H 5.16; N 6.75%.

2-((1–(4-Acetylphenyl)-4–(4-chlorophenyl)-1H-imidazol-2-yl)thio)-1-phenylethan-1-one (22). Synthesis according to the General procedure **D**, using **2** (0.67 g, 2 mmol), and 4′-bromoacetophenone (0.80 g, 4 mmol). Light yellow solid (0.88 g, yield 99%); m.p. 199–200 °C (methanol); IR (KBr) (ν, cm^{-1}): 1611 (C=N); 1670 (2C=O); ^{1}H NMR (400 MHz, DMSO-d_6) δ (ppm): 2.65 (s, 3H, CH_3), 4.84 (s, 2H, CH_2), 7.36 (d, 2H, J=8.6 Hz, H_{Ar}), 7.56 (d, 2H, J=7.8 Hz, H_{Ar}), 7.6–7.74 (m, 5H, H_{Ar}) 8.03 (d, 2H, J=7.7 Hz, H_{Ar}), 8.14 (d, 3H, J=8.3 Hz, H_{Ar}), 8.15 (s, 1H, CH);^{13}C NMR (101 MHz, DMSO-d_6) δ (ppm): 27.4 (CH_3), 40.6 (CH_2), 119.8 (CH), 125.3, 126.4, 128.9, 128.9, 129.2, 130.1, 131.6, 132.6, 134.0, 136.3, 136.7, 140.6 (C–S), 140.7 (CN), 141.9 (C_{Ar}), 194.5 (CH_2C=O), 197.5 (C=O); Anal. Calcd. for $C_{25}H_{19}ClN_2O_2S$: C 67.18; H 4.29; N 6.27%; Found: C 66.98; H 4.42; N 6.09%.

2-((1–(4-Acetylphenyl)-4-phenyl-1H-imidazol-2-yl)thio)-1–(4-chlorophenyl)ethan-1-one (23). Synthesis according to the General procedure **D**, using **1** (0.59 g, 2 mmol), and 2-bromo-4′-chloroacetophenone (0.93 g, 4 mmol).

Bright yellow solid (0.75 g, yield 84%); m.p. 173–174 °C (propan-2-ol); IR (KBr) (v, cm^{-1}): 1613 (C=N); 1682 (2 C=O); ^{1}H NMR (400 MHz, DMSO-d_6) δ (ppm): 2.64 (s, 3H, CH_3), 4.79 (s, 2H, CH_2), 7.21 (t, 1H, *J* = 7.9 Hz, H_{Ar}), 7.30 (t, 2H, *J* = 7.6 Hz, H_{Ar}), 7.56–7.66 (m, 4H, H_{Ar}), 7.69 (d, 2H, *J* = 8.6 Hz, H_{Ar}), 8.04 (d, 2H, *J* = 8.6 Hz, H_{Ar}), 8.09 (s, 1H, CH), 8.12 (d, 2H, *J* = 8.4 Hz, H_{Ar}); ^{13}C NMR (101 MHz, DMSO-d_6) δ (ppm): 27.3 (CH_3), 40.6 (CH_2), 119.3 (CH), 124.76, 125.2, 127.4, 128.9, 129.3, 130.1, 130.8, 133.6, 134.9, 136.6, 138.8, 140.6 (C–S), 141.4 (CN), 141.9 (C_{Ar}), 193.7 (CH_2C=O), 197.5 (C=O); Anal. Calcd. for $C_{25}H_{19}ClN_2O_2S$: C 67.18; H 4.29; N 6.27%; Found: C 66.89; H 4.47; N 6.16%.

2-((1–(4-Acetylphenyl)-4–(4-chlorophenyl)-1H-imidazol-2-yl)thio)-1–(4-chlorophenyl)ethan-1-one (24). Synthesis according to the General procedure **D**, using **2** (0.67 g, 2 mmol), and 2-bromo-4′-chloroacetophenone (0.93 g, 4 mmol). White solid (0.96 g, yield 99.5%); m.p. 189–190 °C (propan-2-ol); IR (KBr) (v, cm^{-1}): 1584 (C=N); 1676 (2 C=O); ^{1}H NMR (400 MHz, DMSO-d_6) δ (ppm): 2.64 (s, 3H, CH_3), 4.79 (s, 2H, CH_2), 7.36 (d, 2H, *J* = 8.4 Hz, H_{Ar}), 7.63 (t, 4H, *J* = 8.2 Hz, H_{Ar}), 7.68 (d, 2H, *J* = 8.4 Hz, H_{Ar}), 8.03 (d, 2H, *J* = 8.4 Hz, H_{Ar}), 8.09–8.17 (m, 3H, H_{Ar}, CH); ^{13}C NMR (101 MHz, DMSO-d_6) δ (ppm): 27.4 (CH_3), 40.6 (CH_2), 119.8 (CH), 125.3, 126.4, 128.9, 129.3, 130.1, 130.8, 131.6, 132.6, 134.9, 136.7, 138.9, 140.5 (C–S), 140.7 (CN), 141.7 (C_{Ar}), 193.7 (CH_2C=O), 197.5 (C=O); Anal. Calcd. for $C_{25}H_{18}Cl_2N_2O_2S$: C 62.38; H 3.77; N 5.82%; Found: C 62.08; H 3.92; N 5.64%.

2-((1–(4-Acetylphenyl)-4-phenyl-1H-imidazol-2-yl)thio)-1–(4-fluorophenyl)ethan-1-one (25). Synthesis according to the General procedure **D**, using **1** (0.59 g, 2 mmol), and 2-bromo-4′-fluoroacetophenone (0.87 g, 4 mmol). White solid (0.85 g, yield 99%); m.p. 162–163 °C (methanol); IR (KBr) (v, cm^{-1}): 1594 (C=N); 1674; 1683 (2 C=O); ^{1}H NMR (400 MHz, DMSO-d_6) δ (ppm): 2.64 (s, 3H, CH_3), 4.81 (s, 2H, CH_2), 7.21 (t, 1H, *J* = 7.3 Hz, H_{Ar}), 7.31 (t, 2H, *J* = 7.9 Hz, H_{Ar}), 7.37 (t, 2H, *J* = 8.7 Hz, H_{Ar}), 7.65 (d, 2H, *J* = 7.7 Hz, H_{Ar}), 7.70 (d, 2H, *J* = 8.2 Hz, H_{Ar}), 8.06–8.18 (m, 5H, H_{Ar}, CH); ^{13}C NMR (101 MHz, DMSO-d_6) δ (ppm): 27.4 (CH_3), 40.7 (CH_2), 116.2 (d, *J* = 21.9 Hz, C-3,5), 119.3 (CH), 124.8, 125.3, 127.4, 128.9, 130.1, 131.9 (d, *J* = 9.5 Hz, C-2,6), 133.0 (d, *J* = 2.8 Hz, C-1), 133.6, 136.6, 140.6 (C–S), 141.4 (CN), 141.9 (C_{Ar}), 165.6 (d, *J* = 252.2, Hz C–F), 193.2 (CH_2C=O), 197.5 (C=O); Anal. Calcd. for $C_{25}H_{19}FN_2O_2S$: C 69.75; H 4.45; N 6.51%; Found: C 69.58; H 4.70; N 6.37%.

2-((1–(4-Acetylphenyl)-4–(4-chlorophenyl)-1H-imidazol-2-yl)thio)-1–(4-fluorophenyl)ethan-1-one (26). Synthesis according to the General procedure **D**, using **2** (0.67 g, 2 mmol), and 2-bromo-4′-fluoroacetophenone (0.87 g, 4 mmol). White solid (0.92 g, yield 99%); m.p. 219–220 °C (propan-2-ol); IR (KBr) (v, cm^{-1}): 1570 (C=N); 1676 (2 C=O); ^{1}H NMR (400 MHz, DMSO-d_6) δ (ppm): 2.65 (s, 3H, CH_3), 4.81 (s, 2H, CH_2), 7.38 (t, 4H, *J* = 7.9 Hz, H_{Ar}), 7.66 (d, 2H, *J* = 8.6 Hz, H_{Ar}), 7.69 (d, 2H, *J* = 8.6 Hz, H_{Ar}), 8.07–8.18 (m, 5H, H_{Ar}, CH); ^{13}C NMR (101 MHz, DMSO-d_6) δ (ppm): 27.4 (CH_3), 40.7 (CH_2), 116.3 (d, *J* = 21.8 Hz, C-3,5), 119.8 (CH), 125.3, 126.4, 128.9, 130.1, 131.6, 131.9 (d, *J* = 9.6 Hz, C-2,6), 132.6, 132.9 (d, *J* = 2.7 Hz, C-1), 136.7, 140.5 (C–S), 140.7 (CN), 141.8 (C_{Ar}), 165.65 (d, *J* = 253.8 Hz, C–F), 193.2 (CH_2C=O), 197.5 (C=O); Anal. Calcd. for $C_{25}H_{18}ClFN_2O_2S$: C 64.58; H 3.90; N 6.03%; Found: C 64.38; H 3.84; N 5.96%.

2-((1–(4-Acetylphenyl)-4-phenyl-1H-imidazol-2-yl)thio)-1–(4-(trifluoromethyl)phenyl)ethan-1-one (27). Synthesis according to the General procedure **D**, using **1** (0.59 g, 2 mmol), and 2-bromo-4′-(trifluoromethyl)acetophenone (1.07 g, 4 mmol). White solid (0.96 g, yield 99.5%); m.p. 195–196 °C (propan-2-ol); IR (KBr) (v, cm^{-1}): 1605 (C=N); 1685 (2 C=O); ^{1}H NMR (400 MHz, DMSO-d_6) δ (ppm): 2.64 (s, 3H, CH_3), 4.83 (s, 2H, CH_2), 7.16–7.22 (m, 1H, H_{Ar}), 7.27 (t, 2H, *J* = 7.3 Hz, H_{Ar}), 7.56 (d, 2H, *J* = 7.4 Hz, H_{Ar}), 7.69 (d, 2H, *J* = 8.2 Hz, H_{Ar}), 7.92 (d, 2H, *J* = 8.0 Hz, H_{Ar}), 8.07–8.15 (m, 3H, H_{Ar}, CH), 8.22 (d, 2H, *J* = 8.0 Hz, H_{Ar}); ^{13}C NMR (101 MHz, DMSO-d_6) δ (ppm): 27.3 (CH_3), 40.6 (CH_2), 119.8 (CH), 122.9, 125.2, 125.6, 126.1 (q, *J* = 3.8 Hz, C-3,5), 126.9 (d, *J* = 272.9 Hz, CF_3), 127.4, 128.9, 129.7, 130.1, 133.1 (d, *J* = 31.9 Hz, C-4), 133.6, 136.6, 139.6, 140.6 (C–S), 141.3 (CN), 141.9 (C_{Ar}), 194.3 (CH_2C=O), 197.5 (C=O); Anal. Calcd. for $C_{26}H_{19}F_3N_2O_2S$: C 64.99; H 3.99; N 5.83%; Found: C 64.68; H 4.11; N 5.77%.

2-((1–(4-Acetylphenyl)-4–(4-chlorophenyl)-1H-imidazol-2-yl)thio)-1–(4-(trifluoromethyl)phenyl)ethan-1-one (28). Synthesis according to the General procedure **D**, using **2** (0.67 g, 2 mmol), and and 2-bromo-4′-(trifluoromethyl)acetophenone (1.07 g, 4 mmol). Light brown solid (1.02 g, yield 99.7%); m.p. 195–196 °C (propan-2-ol); IR (KBr) (v, cm^{-1}): 1599 (C=N); 1690 (2 C=O); ^{1}H NMR (400 MHz, DMSO-d_6) δ (ppm): 2.64 (s, 3H, CH_3), 4.83 (s, 2H, CH_2), 7.32 (d, 2H, *J* = 8.4 Hz, H_{Ar}), 7.58 (d, 2H, *J* = 8.4 Hz, H_{Ar}), 7.68 (d, 2H, *J* = 8.3 Hz, H_{Ar}), 7.92 (d, 2H, *J* = 8.1 Hz, H_{Ar}), 8.12 (d, 2H, *J* = 8.4 Hz, H_{Ar}), 8.14 (s, 1H, CH), 8.20 (d, 2H, *J* = 8.1 Hz, H_{Ar}); ^{13}C NMR (101 MHz, DMSO-d_6) δ (ppm): 27.3 (CH_3), 40.4 (CH_2), 119.8 (CH), 124.2 (d, *J* = 272.6 Hz, CF_3), 125.2,

126.2 (q, J = 3.3 Hz, C-3,5), 126.3, 128.9, 129.7, 130.1, 131.6, 132.5, 133.1 (d, J = 31.9 Hz, C-4), 136.7, 139.6, 140.5 (C–S), 140.7 (CN), 141.6 (C_{Ar}), 194.3 ($CH_2\underline{C}$=O), 197.4 (C = O); Anal. Calcd. for $C_{26}H_{18}ClF_3N_2O_2S$: C 60.64; H 3.52; N 5.44%; Found: C 59.93; H 3.72; N 5.48%.

2-((1–(4-Acetylphenyl)-4-phenyl-1H-imidazol-2-yl)thio)-1–(4-(trifluoromethoxy)phenyl)ethan-1-one (29). Synthesis according to the General procedure **D**, using **1** (0.59 g, 2 mmol), and 2-bromo-4′-(trifluoromethoxy)acetophenone (1.13 g, 4 mmol). White solid (0.98 g, yield 99%); m.p. 167–168 °C (methanol); IR (KBr) (v, cm^{-1}): 1586 (C = N); 1669 (2 C = O); ^{1}H NMR (400 MHz, DMSO-d_6) δ (ppm): 2.64 (s, 3H, CH_3), 4.81 (s, 2H, CH_2), 7.20 (t, 1H, J = 7.3 Hz, H_{Ar}), 7.28 (t, 2H, J = 7.5 Hz, H_{Ar}), 7.53 (d, 2H, J = 8.3 Hz, H_{Ar}), 7.61 (d, 2H, J = 7.7 Hz, H_{Ar}), 7.70 (d, 2H, J = 8.2 Hz, H_{Ar}), 8.09 (s, 1H, CH), 8.13 (d, 2H, J = 8.3 Hz, H_{Ar}), 8.17 (d, 2H, J = 8.5 Hz, H_{Ar}); ^{13}C NMR (101 MHz, DMSO-d_6) δ (ppm): 27.3 (CH_3), 40.5 (CH_2), 119.3 (CH), 121.2, 121.7, 124.7, 125.2, 127.3, 128.9, 130.1, 131.4, 133.6, 135.2, 136.6, 140.6 (C–S), 141.4 (CN), 141.8, 152.1 (C_{Ar}), 193.5 ($CH_2\underline{C}$=O), 197.5 (C = O); Anal. Calcd. for $C_{26}H_{19}F_3N_2O_3S$: C 62.90; H 3.86; N 5.64%; Found: C 62.75; H 4.00; N 5.61%.

2-((1–(4-Acetylphenyl)-4–(4-chlorophenyl)-1H-imidazol-2-yl)thio)-1–(4-(trifluoromethoxy)phenyl)ethan-1-one (30). Synthesis according to the General procedure **D**, using **2** (0.67 g, 2 mmol), and 2-bromo-4′-(trifluoromethoxy)acetophenone (1.13 g, 4 mmol). Light orange solid (1.04 g, yield 99%); m.p. 191–192 °C (propan-2-ol); IR (KBr) (v, cm^{-1}): 1601 (C = N); 1684 (2 C = O); ^{1}H NMR (400 MHz, DMSO-d_6) δ (ppm): 2.64 (s, 3H, CH_3), 4.82 (s, 2H, CH_2), 7.34 (d, 2H, J = 8.4 Hz, H_{Ar}), 7.53 (d, 2H, J = 8.4 Hz, H_{Ar}), 7.63 (d, 2H, J = 8.4 Hz, H_{Ar}), 7.69 (d, 2H, J = 8.3 Hz, H_{Ar}), 8.13 (d, 2H, J = 8.3 Hz, H_{Ar}), 8.15 (s, 1H, CH), 8.16 (d, 2H, J = 8.4 Hz, H_{Ar});^{13}C NMR (101 MHz, DMSO-d_6) δ (ppm): 27.3 (CH_3), 40.6 (CH_2), 119.8 (CH), 121.2, 125.3, 126.4, 128.9, 130.1, 131.4, 131.6, 132.6, 135.2, 136.7, 140.5 (C–S), 140.7 (CN), 141.7, 152.2 (C_{Ar}), 193.5 ($CH_2\underline{C}$=O), 197.4 (C = O); Anal. Calcd. for $C_{26}H_{18}ClF_3N_2O_3S$: C 58.82; H 3.42; N 5.28%; Found: C 59.16; H 3.56; N 5.61%.

Biological evaluation

Cell culture

In this study, six human cancer cell lines were used: A-549 (lung adenocarcinoma, ATCC® CCL-185™), NCI-H-226 (lung squamous cell carcinoma, ATCC® CRL-5826™), NCI-H-460 (large cell lung carcinoma, ATCC® HTB-177™), HCT116 (colorectal carcinoma, ATCC® CCL-247™), Hep G2 (hepatocellular carcinoma, ATCC® HB-8065™), and HeLa (cervical carcinoma, ATCC® CCL-2™). To assess the selectivity of the compounds, two non-cancerous human cell lines, HaCaT (immortalised human keratinocytes, CLS Cat. No. 300493) and MRC-5 (normal human lung fibroblasts, ATCC® CCL-171™), were also included.A-549, NCI-H-226, and NCI-H-460 cells were cultured in RPMI-1640 medium (Corning), while HCT116 cells were maintained in McCoy's 5 A medium (Corning). Hep G2 and HeLa cells, as well as HaCaT keratinocytes, were cultured in Dulbecco's Modified Eagle Medium (DMEM; Corning), and MRC-5 fibroblasts were maintained in Minimum Essential Medium (MEM; Corning). All media were supplemented with 10% foetal bovine serum (FBS; Corning), 2 mM L-glutamine (Corning), and antibiotics (100 U/mL penicillin and 100 µg/mL streptomycin; Sigma-Aldrich). All cell lines were grown at 37 °C in a humidified incubator with 5% CO_2. Cells were passaged at 70–80% confluency using standard trypsinization protocols, and mycoplasma contamination was routinely monitored using PCR-based detection methods.

Cell viability assay

Cell viability was assessed using the MTT assay (3–(4,5-dimethylthiazol-2-yl)-2,5-diphenyltetrazolium bromide; Sigma-Aldrich). Cells were seeded into 96-well plates and allowed to adhere overnight. Subsequently, they were treated with various concentrations (0–50 µM) of the test compounds for 72 h. Cells treated with DMSO served as a vehicle control. Following treatment, 0.4 mg/mL MTT solution was added to each well and incubated for an additional 2–3 h at 37 °C. After incubation, the medium was carefully removed, and 100 µL of DMSO was added to dissolve the formazan crystals. Absorbance was measured at 450 nm using an ASYS UVM340 microplate reader. The half-maximal inhibitory concentration (IC_{50}) values were calculated from dose-response curves generated using GraphPad Prism 9 software. All experiments were performed in triplicate, and the results are presented as the mean values from three independent experiments to ensure reproducibility and reliability.

Cell cycle analysis

A-549 cell line was seeded onto appropriate culture plates and allowed to adhere overnight under standard culture conditions. Following adhesion, cells were treated with the tested compounds for either 24 or 48 h. After treatment, the cells were fixed in 75% ice-cold ethanol and stored at −20 °C overnight. Prior to analysis, the fixed cells were washed twice with phosphate-buffered saline (PBS; Sigma-Aldrich) and centrifuged. The cells were then stained with a solution of propidium iodide (20 µg/mL; Sigma-Aldrich) and RNase A (50 µg/mL; Sigma-Aldrich) in PBS, and incubated at room temperature for 30 min in the dark. Cell cycle distribution was subsequently determined using a Guava easyCyte 8 flow cytometer (Merck Millipore), and data were analysed with FlowJo v10 software (BD Life Sciences).

Apoptosis and caspase 3/7 activation

For the assessment of apoptosis, A-549 cells were seeded onto tissue culture plates and incubated overnight to allow adherence. On the following day, cells were exposed to the tested compounds for 24 or 48 h, with etoposide (ETP; Sigma-Aldrich) used as a positive control. After treatment, cells were harvested by trypsinization, washed twice with PBS, and stained according to the manufacturers' instructions. Apoptotic cells were labelled using an Annexin V-FITC conjugate (Thermo Fisher Scientific; #A13199), while caspase-3/7 activity was detected using the CellEvent™ Caspase-3/7 Green Flow Cytometry Assay Kit (Thermo Fisher Scientific, #C10427). The stained cells were subsequently analysed by flow cytometry using a Guava easyCyte 8 cytometer (Merck Millipore), and data were processed with FlowJo v10 software (BD Life Sciences).

Mitochondrial membrane potential

To evaluate mitochondrial membrane potential (ΔΨm), A-549 cells were seeded onto tissue culture plates and allowed to adhere overnight. The following day, cells were treated with compound **24** for 6 or 24 h. Carbonyl cyanide-p-trifluoromethoxyphenylhydrazone (FCCP; 10 µM; Sigma-Aldrich) was used as a positive control for mitochondrial depolarisation and was added 30 min before the end of incubation. Following treatment, the culture medium was replaced with fresh medium containing JC-1 dye (5 µg/mL; Sigma-Aldrich), and cells were incubated at 37 °C for 20 min in the dark. After staining, cells were washed twice with PBS and analysed by flow cytometry using a Guava easyCyte 8 cytometer (Merck Millipore). Data were processed with FlowJo v10 software (BD Life Sciences). JC-1 monomeric (green fluorescence) and aggregate (red fluorescence) signals were quantified, and the red/green fluorescence intensity ratio was used as an indicator of mitochondrial membrane integrity.

Reactive oxygen species detection

For the assessment of intracellular reactive oxygen species (ROS), A-549 cells were seeded onto tissue culture plates and allowed to adhere overnight. Cells were then treated with compound **24** for 1, 3, 6, or 24 h. Hydrogen peroxide (H_2O_2; 10 µM, Sigma-Aldrich) was used as a positive control for ROS induction, and N-acetylcysteine (NAC; 5 mM; Sigma-Aldrich) was used as an antioxidant control. Thirty minutes before the end of each treatment time point, 1 µM CM-H_2DCFDA probe (5-(and-6)-chloromethyl-2′,7′-dichlorodihydrofluorescein diacetate, acetyl ester; #C6827; Thermo Fisher Scientific) was added directly to the culture medium. After staining, cells were harvested using 0.05% trypsin in PBS and Hank's Balanced Salt Solution, washed twice with PBS, and stained with 7-AAD (7-Aminoactinomycin D; Sigma-Aldrich) to exclude dead cells. Fluorescence intensity was measured by flow cytometry using a Guava easyCyte 8 cytometer (Merck Millipore), and data were analysed using FlowJo v10 software (BD Life Sciences).

Evaluation of DNA Double-Strand break (DSB) induction

For the assessment of DNA damage, A-549 cell line was seeded onto tissue culture plates and incubated overnight to allow adherence. The following day, cells were treated with the tested compounds for 24 or 48 h, with mitoxantrone (1 µM; Sigma-Aldrich) included as a positive control. After incubation, cells were collected by trypsinization, fixed in 75% ethanol, and stored at − 20 °C until further use. For analysis, the cells were rehydrated with PBS on ice for 5 min, followed by permeabilization with 0.2% Triton X-100 in PBS

at room temperature for 15 min. Subsequently, cells were incubated with Alexa Fluor 488-conjugated mouse anti-phospho-γH2AX (Ser139) antibody (#613406; BioLegend) diluted 1:200, and maintained at 37 °C for 1.5 h. After washing with PBS, the cells were counterstained with propidium iodide (20 µg/mL) and RNase A (50 µg/mL) for 30 min. The fluorescence signals were measured using a Guava easyCyte 8 flow cytometer (Merck Millipore), and data analysis was performed using FlowJo v10 software.

Wound healing migration assay

The antimigratory properties of compound **24** were evaluated using a wound healing assay. A-549 cells were seeded into Ibidi silicone inserts placed on glass-bottom 24-well plates suitable for live-cell imaging and incubated overnight at 37 °C in a humidified atmosphere containing 5% CO_2. After incubation, the inserts were gently removed, and cellular debris was eliminated by washing twice with fresh RPMI medium. To inhibit cell proliferation and ensure that observed effects were due solely to cell migration, the cells were pre-treated with 10 µg/mL mitomycin C (Sigma-Aldrich) for 1 h, followed by two additional washes with fresh medium. Subsequently, cells were treated with various concentrations of compound **24** (5, 10, 15 µM), selected based on previous experimental data indicating no cytotoxicity at the tested concentrations after 24 h of treatment. In some experiments, cells were also stimulated with 2.5 ng/mL of TGF-β1 (Transforming Growth Factor beta 1; Sigma-Aldrich) to promote migration. The plates were transferred into an imaging chamber (cellVivo incubation system; Olympus) maintained at 37 °C with 5% CO_2. Live-cell imaging was conducted using a phase-contrast fluorescence microscope (IX83 Inverted Microscope, Olympus) connected to an XC50 digital colour camera (Olympus). Time-lapse images were acquired every hour over a 24-h period at ×10 magnification. The acquired images were assembled into time-lapse videos using cellSens software (Olympus), and the wound gap areas were quantified using ImageJ software (NIH).

Matrigel invasion assay

Cell invasive ability was assessed using a Matrigel-based Transwell invasion assay, following the procedure adapted from Pijuan et al. with modifications.[25] Briefly, Transwell inserts with an 8 µm pore size (Corning) were placed into 24-well plates and coated with 50 µL of Matrigel (Corning) diluted 1:3 in serum-free medium. The inserts were incubated at 37 °C for 1 h to allow the Matrigel to polymerise. After Matrigel solidification, cells were harvested by trypsinization, resuspended in serum-free medium, and seeded at a density of 1×10^5 cells in 200 µL into the upper chamber of each insert. The lower chamber was filled with 600 µL of complete medium containing 10% foetal bovine serum (FBS) as a chemoattractant. Cells were treated with selected non-cytotoxic concentrations of the test compounds immediately after seeding. Untreated cells were included as the negative control. The plates were incubated at 37 °C in a humidified atmosphere containing 5% CO_2 for 24 h. Following incubation, non-invading cells on the upper surface of the membrane were carefully removed using a cotton swab. Cells that had migrated through the Matrigel and adhered to the underside of the membrane were fixed with 4% paraformaldehyde for 20 min at room temperature. Subsequently, cells were stained with Hoechst 33342 dye (Thermo Fisher Scientific) at a final concentration of 5 µg/mL for 15 min at room temperature, protected from light. Stained cells were visualised using a fluorescence microscope (Olympus IX83), and images were captured from four randomly selected fields per insert. The number of invaded cells was quantified using ImageJ software (NIH). Results were expressed as the mean number of invading cells per field from three independent experiments.

RNA extraction

Cells were seeded at a density of 1.5×10^6 cells per well onto tissue culture plates and allowed to adhere overnight under standard conditions. Following a 24-h incubation, cells were treated with compounds or 1% (v/v) DMSO for the indicated durations. After treatment, cells were washed twice with PBS to remove residual medium and subsequently lysed using TRIzol Reagent (Thermo Fisher Scientific). The lysates were stored at −80 °C until further processing. Total RNA was extracted using the Total RNA Zol-Out kit (#043–100; A&A Biotechnology) according to the manufacturer's protocol. The concentration of isolated RNA was determined by measuring the absorbance at 260 nm using a NanoDrop ND-1000

spectrophotometer (Thermo Fisher Scientific). RNA purity was assessed by calculating the A260/A280 absorbance ratio, with values close to 2.0 considered indicative of high purity.

Analysis of genes expression by RT-PCR

The expression of *MMP2*, *MMP9* and *hTERT* was analysed using reverse transcription followed by quantitative PCR (RT-qPCR). First-strand cDNA was synthesised from total RNA using the PrimeScript RT reagent kit with gDNA Eraser (#RR047B;TaKaRa), according to the manufacturer's protocol. The cDNA synthesis procedure involved an initial genomic DNA elimination step at 42 °C for 2 min, followed by reverse transcription at 37 °C for 15 min, and enzyme inactivation at 85 °C for 5 s. Quantitative PCR was performed using TB Green Premix Ex Taq II (#RR82WR;TaKaRa) on a LightCycler 480 system (Roche Life Science). The qPCR cycling conditions were as follows: an initial denaturation at 95 °C for 30 s, followed by 45 amplification cycles of 95 °C for 5 s and 60 °C for 60 s, and a final denaturation at 96 °C for 5 s. Melting curve analysis was carried out by increasing the temperature from 60 °C to 95 °C with a ramp rate of 0.5 °C every 2 s to verify the specificity of amplification products. Primer sequences used for all genes are provided in Table 1. Relative gene expression levels were calculated using the comparative ΔΔCt method, with DMSO-treated cells serving as the control group. All experiments were performed in biological triplicates to ensure reproducibility.

3D spheroid formation assay

Three-dimensional spheroids were generated using the 3D Petri Dish® system (MicroTissues®; #12–256) in accordance with the manufacturer's recommendations. A 2% agarose solution in normal saline was sterilised, liquefied by heating, and cast into the moulds under aseptic conditions. After solidification at room temperature, the agarose micromolds were transferred to 12-well plates and equilibrated with culture medium. Cells were seeded onto the moulds in serum-free medium and allowed to settle into microwells for 1–2 h at 37 °C. Additional medium was then added to fully immerse the gels. Following spheroid formation, cells were treated with compound **24** at concentrations of 10 µM, 25 µM, or 50 µM, or with vehicle control (0.5% v/v DMSO in PBS). The spheroids were maintained in a humidified incubator at 37 °C and monitored continuously for 72 h. Bright-field images were acquired every 30 min using an Olympus CellVivo inverted microscope equipped for long-term live-cell imaging. Quantitative analysis of spheroid morphology was conducted with Olympus CellSens software.

In ovo CAM assay

The anti-metastatic activity of compound **24** was assessed using the *in ovo* chorioallantoic membrane (CAM) model, following a modified protocol adapted from Rodrigo *et al.*[26] Fertilised chicken eggs were incubated at 37.5 °C with 65% relative humidity and gentle rotation for 10 days. On day 10, a small aperture was created at the blunt pole of each egg (air sac region) using a 30-gauge needle. A second hole was then drilled near a prominent allantoic vein under visual control using a Dremel rotary tool (Dremel, Racine). To facilitate membrane detachment, a mild vacuum was applied to the air sac via an automated pipette connected to Tygon tubing. A window (~1 cm^2) was carefully cut with a Dremel cut-off wheel above the bifurcation of the allantoic vessels, providing direct access to the CAM. For xenografting, A-549 cells were pre-stained with CellTracker Green (Invitrogen). A suspension containing 4×10^6 A-549 cells in 25 µL of medium was gently deposited near the allantoic vein bifurcation. Following a settling period of 5–10 min in an upright position, the openings were sealed with adhesive tape, and the eggs were returned to stationary incubation at 37.5 °C for 5 days. After tumour establishment, 25 µM or 50 µM solutions of compound **24**, or vehicle control (0.5% v/v DMSO in PBS), were

Table 1. Primer sequences used for RT-PCR (5′-3′).

Gene	Forward Primer	Reverse Primer
RPII	CTTCACGGTGCTGGGCATT	GTGCGGCTGCTTCCATAA
hTERT	CATCAGGGGCAAGTCCTACG	AAGTTCACCACGCAGCCATA
MMP-9	ATGTACCCTATGTACCGCTTCACT	CAGAGAAGAAGAAAAGCTTCTTGG
MMP-2	GAAGTATGGGAACGCCGATGG	TTGTCGCGGTCGTAGTCCTCA

applied topically onto the developing microtumors. Subsequent incubation proceeded for an additional 48 h. To visualise blood vessels, 50 µL of Lens culinaris agglutinin (LCA; 10 µg/mL; Vector Laboratories) was administered into peripheral CAM veins using a 30-gauge hypodermic needle attached to a 1 ml syringe. CAM tissues were excised and fixed in 4% paraformaldehyde in PBS (PFA, Sigma-Aldrich). Tumour morphology and vascularisation were documented using both bright-field stereomicroscopy (Olympus SZX7) and fluorescence microscopy (IX83 Inverted Microscope, Olympus) under standardised imaging parameters. Quantitative analyses, including measurement of tumour area and mean fluorescence intensity, were performed with Fiji software employing threshold-based segmentation methods to eliminate background signals. All experiments complied with the European Directive 2010/63/EU, under which CAM assays are not classified as animal experiments (European Commission, 2021/2784(RSP)).

MMP-9 inhibition assay

The inhibitory activity of the tested compounds against MMP-9 was evaluated using the MMP-9 Inhibitor Screening Assay Kit (Fluorometric) (Abcam, ab139449) following the manufacturer's instructions. Briefly, assays were performed in 96-well half-area microplates with a final reaction volume of 100 µL per well. Recombinant human MMP-9 enzyme was diluted in the supplied assay buffer and added at 20 µL/well to give a final concentration of 0.9 U. The fluorogenic substrate Mca-Pro-Leu-Gly-Leu-Dpa-Ala-Arg-NH_2 was added at a final concentration of 4 µM to initiate the reaction. Test compounds were prepared by two-fold serial dilution in assay buffer to give in-assay concentrations ranging from 100 to 0.39 µM. The reference inhibitor NNGH (N-Isobutyl-N-(4-methoxyphenylsulfonyl)glycyl hydroxamic acid, supplied with the kit, was used as a positive control at concentrations from 1.0 to 0.0156 µM. Control wells without inhibitor were included to define 100% enzyme activity. Following 30 min pre-incubation of enzyme with inhibitors at 37 °C, reactions were started by substrate addition. Fluorescence was monitored kinetically at λ_ex = 328 nm and λ_em = 420 nm every 60 s for 10 min using a microplate reader. Initial reaction velocities were determined from the linear portion of each progress curve, and percent remaining activity was calculated relative to uninhibited control reactions. IC_{50} values were obtained by nonlinear regression analysis of inhibitor concentration versus residual activity.

Molecular docking and MD simulation

The X-ray crystal structures of matrix metalloproteinase-3 (MMP-3, PDB ID 7XJO) and matrix metalloproteinase-9 (MMP-9, PDB ID 5CUH) were obtained from the Protein Data Bank. Each structure was processed with the Protein Preparation Wizard in Schrödinger Maestro v12.8: all crystallographic water molecules were removed, missing side-chains and loops were rebuilt with Prime, hydrogen atoms were added, and the resulting models were energy-minimised using the OPLS-2005 force field. All ligands were generated with LigPrep (Schrödinger) to produce the lowest-energy protonation and tautomeric states at pH 7.0 ± 0.5, and subsequently minimised with the OPLS-2005 force field. Molecular docking was carried out with the GLIDE module (Maestro v12.8) in extra-precision (XP) mode. To allow limited steric relaxation, the van der Waals radii of non-polar atoms were scaled to 0.8 (corresponding to a 0.15 partial-charge cut-off). Default grid sizes centred on the co-crystallised ligands were used. For each ligand, the ten highest-ranking poses were retained. Docking poses and intermolecular contacts were inspected in PyMOL v3.1, and XP scoring functions were used for ranking. The top-scoring protein–ligand complexes were embedded in an orthorhombic TIP3P water box with a 10 Å buffer in Desmond (Schrödinger). Na^+/Cl^- ions were added to achieve charge neutrality and a physiological salt concentration of 150 mM. After an automated relaxation protocol, 500 ns production runs were performed under isothermal–isobaric (NPT) conditions at 300 K and 1 bar, maintained with the Nose–Hoover thermostat and Martyna–Tobias–Klein barostat. The simulation trajectories were analysed with the Desmond Simulation Interaction Diagram tool. Root meansquare deviation (RMSD) and rootmean-square fluctuation (RMSF) profiles were calculated for Cα atoms, while hydrogen bonds and other protein–ligand interactions were monitored over time to assess complex stability and validate the docking results.

Results

Chemistry

In continuation of our previous research on the synthesis and evaluation of biological properties of imidazole derivatives,[24] in this study we extended the scope of this synthesis to obtain variously S-substituted imidazolethione derivatives **6–30**, whose preparation sequences are depicted in Scheme 2. Firstly, the initial compounds **1–5** from the previous study were subjected to the action of methyl bromoacetate. The reaction at reflux of 2 equiv. of thioxoimidazoles**1 – 5** with 4 equiv. of alkylating agent in methanol and in the presence of anhydrous potassium carbonate as a base, led to the formation of S-alkylated derivatives **6 – 10** in good to excellent yield of 74 – 98%.

Reagents and conditions: i methyl 2-bromoacetate (for **6–10**), 1-chloropropan-2-one (for **16–20**) or the corresponding bromoacetophenone (for **21–30**), MeOH, anhydrous K_2CO_3, Δ, 1–2 h; *ii* 18.5% HCl, Δ, 1 h.

1, **6**, **11**, **16** R^1 = H; **2**, **7**, **12**, **17** R^1 = Cl; **3**, **8**, **13**, **18** R^1 = OH; **4**, **9**, **14**, **19** R^1 = F; **5**, **10**, **15**, **20** R^1 = NO_2; **21** R^1 = R^2 = H; **22** R^1 = Cl, R^2 = H; **23** R^1 = H, R^2 = Cl; **24** R^1 = R^2 = Cl; **25** R^1 = H, R^2 = F; **26** R^1 = Cl, R^2 = F; **27** R^1 = H, R^2 = CF_3; **28** R^1 = Cl, R^2 = CF_3; **29** R^1 = H, R^2 = OCF_3; **30** R^1 = Cl, R^2 = OCF_3.

The structure of the synthesised compounds **6 – 30** was characterised by spectral data (IR, NMR spectra, and elemental analysis). The spectra showed good agreement with the assigned molecular structures. In the ^{1}H NMR spectra, the obtained compounds **6 – 10** showed a singlet signal in the range of 4.06–4.19 ppm, corresponding to the CH_2 group protons of the newly formed SCH_2COOCH_3 fragment. The signal of the methoxy protons resonated at approx. 3.65 ppm. In the ^{13}C NMR spectra, the resonance line of the carbon of the C=O group, incorporated in the CH_2COOCH_3 fragment, was observed at approx. 169.6 ppm. Also, the ^{13}C NMR spectra demonstrated altered chemical shifts from 163 ppm for C=S[24] towards approx. 140.5 ppm for C – S.

To obtain carboxylic acids **11 – 15**, the hydrolysis of methyl esters **6 – 10** was carried out. The reaction was catalysed by dilute hydrochloric acid. The reflux of the corresponding compound **6 – 10** with a large excess of water containing a strong-acid catalyst, resulted in the demethylated derivatives **11 – 15**. The differences in the NMR spectra of compounds **6 – 10** and **11 – 15** confirmed the formation of the COOH group. In the ^{13}C NMR spectra of the latter, the carbon resonance of the COOH group was shifted down-field if compared to the ester spectra. The absence of the OCH_3 peak (^{1}H NMR) and the appearance of a broad singlet integrated for 1H in the downfield of the spectra correspond to the OH group of the COOH, which supports molecular structure of compounds **11 – 15**.

Next, new S-substitutions were carried out by using α-halo ketones – 1-chloropropan-2-one and bromoacetophenones. Compounds **1 – 5**, when treated with 1-chloropropan-2-one, also known as chloroacetone, at the same conditions as for **6 – 10,** produced compounds **16 – 20** having thiopropan-2-one fragment in 70 – 99% yield. In the NMR spectra, new peaks at about 2.28 ppm, and between 4.16 and 4.25 ppm (^{1}H NMR) for the protons of the CH_3COCH_2S fragment, and resonance lines at 27.36 (CH_3),

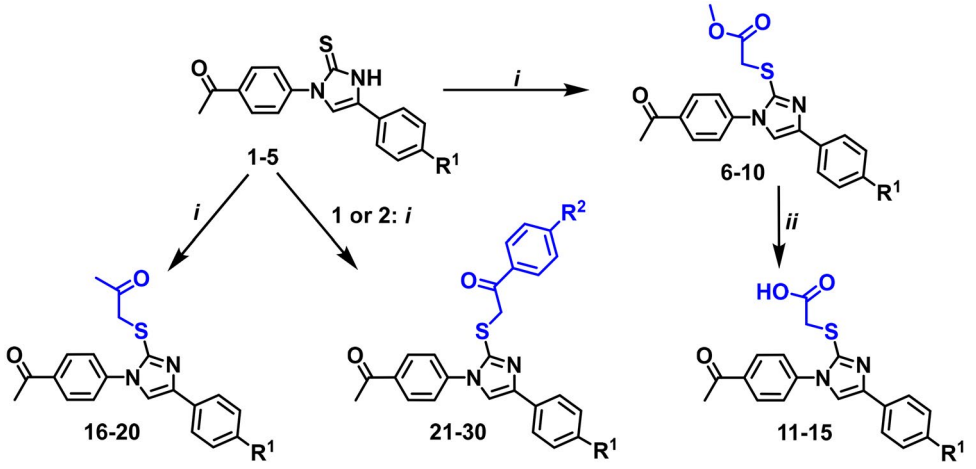

Scheme 2. Synthesis pathways of imidazole derivatives **6 – 30**

43.65 – 43.86 (CH_2), and 202.77 – 203.10 (C = O) ppm for the carbons of the same fragment (^{13}C NMR) approved its existence. The protons of the phenyl rings were observed in the aromatic proton region between 6.78 and 8.27 ppm, while the imidazole CH group proton peak resonated in the 7.88 – 8.41 ppm range.

Ultimately, one more series of S-substituted imidazoles **21 – 30** was prepared as a result of the interaction of compounds **1** or **2** with the corresponding bromoacetophenone at the same conditions as for **6 – 10**, and **16 – 20**. The reaction occurred easily, and the desired SCH_2COAr fragment was constructed in a 2-h long reaction, and crystalline products were isolated in an excellent yield of 84 – 99.7%. The NMR spectra revealed peaks ranging from 4.79 to 4.84 ppm (^1H) and from 40.51 to 40.74 ppm (^{13}C) for CH_2 group, and carbon peaks of C – S group were found to resonate in upper field of the spectra at approx. 140.6 ppm if compared to C = S for **1 – 5**, which resonated at approx. 160 ppm. Furthermore, additional peaks of new aryl moieties were observed in the ^1H and ^{13}C NMR spectra. The remaining spectral lines were in good agreement with the molecular structures of compounds **21 – 30**.

Biological evaluation

Cell cytotoxic evaluation

The antiproliferative activity of the of S-substituted imidazole-2-thione derivatives was assessed by the MTT assay after 72 h of exposure against a panel of human cancer cell lines, including lung adenocarcinoma (A-549), lung squamous cell carcinoma (H-226), large cell lung carcinoma (H-460), colorectal carcinoma (HCT-116), hepatocellular carcinoma (Hep G2), and cervical carcinoma (HeLa). To preliminarily assess the potential selectivity of the compounds, two non-cancerous cell lines were also included: immortalised human keratinocytes (HaCaT) and normal human lung fibroblasts (MRC-5). The IC_{50} values obtained are summarised in Table 2.

Table 2. *In vitro* anticancer activity of investigated compounds (IC_{50} ± SD (μM)).

Compound	A-549	H-226	H-460	HCT-116	Hep G2	HeLa	HaCaT	MRC-5	SI[b]
	IC_{50} values [μM][a]								
1	>100	>100	>100	>100	>100	>100	>100	>100	ND
2	>100	>100	>100	>100	>100	>100	>100	>100	ND
3	40.53 ± 2.6	56.45 ± 20.09	72.99 ± 8.23	>100	>100	36.49 ± 4.16	69.42 ± 7.26	>100	ND
4	>100	>100	>100	>100	>100	>100	>100	>100	ND
5	>100	>100	>100	>100	>100	>100	>100	>100	ND
6	>100	>100	>100	>100	>100	>100	>100	>100	ND
7	>100	>100	>100	>100	>100	>100	93.38 ± 9.65	>100	ND
8	47.85 ± 7.61	47.04 ± 16.78	47.34 ± 14.44	68.05 ± 0.62	67.59 ± 2.89	23.67 ± 7.21	55.05 ± 6.26	62.21 ± 4.23	1.31
9	>100	>100	>100	>100	>100	>100	>100	>100	ND
10	>100	>100	>100	>100	>100	>100	>100	>100	ND
11	>100	>100	>100	>100	>100	>100	>100	>100	ND
12	>100	>100	>100	>100	>100	>100	>100	>100	ND
13	>100	>100	>100	>100	>100	>100	>100	>100	ND
14	>100	>100	>100	>100	>100	>100	>100	>100	ND
15	>100	>100	>100	>100	>100	>100	>100	>100	ND
16	76.62 ± 6.29	>100	>100	>100	85.23 ± 5.23	>100	99.58 ± 7.65	>100	ND
17	74.67 ± 7.81	29.89 ± 3.64	31.04 ± 7.35	>100	23.07 ± 1.26	15.52 ± 3.67	>100	>100	ND
18	38.94 ± 8.21	44.73 ± 6.36	44.39 ± 5.23	>100	92.98 ± 3.26	22.19 ± 2.89	73.33 ± 6.02	>100	ND
19	54.88 ± 6.09	76.89 ± 21.36	88.15 ± 7.35	>100	84.61 ± 8.85	44.08 ± 3.26	92.79 ± 6.91	75.34 ± 6.32	1.03
20	>100	>100	>100	>100	>100	>100	>100	>100	ND
21	11.76 ± 7.66	7.92 ± 3.27	14.48 ± 0.31	39.89 ± 18.55	31.84 ± 3.25	7.24 ± 0.15	19.71 ± 5.23	44.88 ± 5.54	3.94
22	34.34 ± 34.11	>100	>100	29.19 ± 17.24	>100	>100	23.55 ± 6.34	>100	ND
23	7.01 ± 3.75	2.12 ± 0.44	2.09 ± 0.10	26.02 ± 5.58	25.76 ± 3.27	1.05 ± 0.05	13.00 ± 2.03	10.48 ± 2.02	2.8
24	**2.23 ± 0.07**	**2.34 ± 0.08**	**5.49 ± 3.19**	**4.95 ± 7.56**	**51.41 ± 6.26**	**2.75 ± 1.59**	**8.89 ± 0.52**	**18.47 ± 4.23**	**4.28**
25	35.04 ± 7.69	12.41 ± 0.22	46.24 ± 12.51	>100	88.94 ± 6.33	>100	>100	50.97 ± 6.23	1.63
26	7.05 ± 0.13	3.03 ± 1.07	16.24 ± 9.39	>100	>100	4.69 ± 1.22	6.58 ± 0.46	33.88 ± 3.14	3.86
27	>100	>100	>100	>100	>100	>100	>100	>100	ND
28	>100	3.23 ± 1.01	6.92 ± 1.57	53.85 ± 28.75	54.31 ± 5.22	3.46 ± 0.78	15.69 ± 3.33	1.77 ± 0.29	0.35
29	>100	>100	>100	>100	>100	>100	>100	>100	ND
30	>100	>100	>100	>100	>100	>100	>100	>100	ND
Cisplatin	29.01 ± 0.12	17.47 ± 2.12	21.49 ± 1.87	24.89 ± 1.14	15.87 ± 1.89	25.23 ± 2.16	21.34 ± 3.09	56.23 ± 4.65	2.53

">100" indicates that no measurable cytotoxicity was observed at concentrations up to 100 μM; "ND" (not determined) indicates that the IC_{50} value could not be calculated because the compound did not exhibit inhibitory activity under the experimental conditions.

[a]IC_{50} value represent a concentration that inhibits 50% of cell growth.

[b]SI value represent selectivity indexes (IC_{50} MRC-5/Average IC_{50} cancer cell lines).

The majority of the tested compounds exhibited limited or no antiproliferative activity, with IC_{50} values above 100 µM in all cancer cell lines. Notable exceptions were found among hydroxyl- and chloro-substituted derivatives, as well as members of the bromoacetophenone series. Compounds **3** and **8**, bearing hydroxyl substituents, showed moderate cytotoxicity. Compound **3** inhibited proliferation of A-549, H-226, H-460, and HeLa cells with IC_{50} values between 36.49 and 72.99 µM, while compound **8** exerted broader effects, with IC_{50} values in the range of 23.67–68.05 µM across all tested tumour models.

Among the propan-2-one derivatives, compounds **17** and **18** demonstrated the most consistent activity. Compound **17** was active against H-226, H-460, HepG2, and HeLa cells, with IC_{50} values of 15.52–31.04 µM, whereas compound **18** displayed activity in a similar range (22.19–44.73 µM). In contrast, compounds **16** and **19** were weakly active, with IC_{50} values exceeding 70 µM.

The most pronounced cytotoxicity was observed in the bromoacetophenone series. Compound **21** (unsubstituted) displayed low-micromolar activity in lung carcinoma and HeLa cells (7.24–14.48 µM). Compound **23** (H, Cl) exhibited sub- to low-micromolar potency across multiple lines, with IC_{50} values of 1.05–7.01 µM, and compound **24** (Cl, Cl) emerged as the most active derivative, achieving IC_{50} values of 2.23–5.49 µM in A-549, H-226, and HeLa cells. Compound **26** (Cl, F) was also highly active, with IC_{50} values of 3.03–16.24 µM. In contrast, analogues containing strongly electron-withdrawing substituents such as NO_2, CF_3, or OCF_3 (compounds **5**, **10**, **15**, **20**, **27**, **29**, and **30**) were completely inactive. Compound **28** (Cl, CF_3) showed low-micromolar IC_{50} values in H-226 and H-460 (3.23 and 6.92 µM, respectively), but was also cytotoxic to MRC-5 fibroblasts, indicating reduced selectivity. Compound **22** exhibited selective, moderate activity against colorectal carcinoma HCT-116 ($IC_{50} \approx 29.19$ µM), whereas compound **25** produced moderate effects in lung carcinoma models (12.41–46.24 µM).

Although the HaCaT cell line was included to provide supplementary information regarding compound cytotoxicity, it was not used for the calculation of the selectivity index (SI) due to its immortalised nature and associated genetic alterations. Thus, SI values reported in this study are based exclusively on MRC-5 normal human fibroblasts, and should be interpreted as preliminary indicators rather than definitive measures of selectivity.

Based on its superior potency and preliminary evidence of a therapeutic window, compound **24** was selected for further biological studies. Although additional non-malignant cell types will be required to rigorously define its safety profile, the SI value of compound **24**—approximately 1.7-fold higher than that of cisplatin—suggests that it may hold promise as a candidate for further development.

Cell cycle analysis following compound treatment in A-549 cells

To delineate the effects of compound **24** on cell cycle progression, A-549 cells were exposed to DMSO (vehicle control), etoposide (ETP; reference compound), or compound **24** at their respective IC_{50} concentrations for 24, 48, and 72 h. Cell cycle profiles were analysed by flow cytometry, and the relative distribution of cells in G1, S, and G2/M phases was quantified (Figure 2).

At the 24-h time point, both ETP and compound **24** elicited a significant decrease in the S-phase population compared to DMSO-treated controls ($p \leq 0.001$ for ETP; $p \leq 0.01$ for **24**), indicating an early perturbation of DNA synthesis (Figure 1(a) and (b)). No statistically significant alterations were observed in the G1 compartment for either agent at this time (Figure 1(b)). A modest but significant increase in the G2/M fraction was detected in the ETP-treated group ($p \leq 0.05$), while compound **24** had no discernible impact on this phase at this stage (Figure 1(b)).

By 48 h, cells treated with compound **24** exhibited a statistically significant accumulation in the G1 phase ($p \leq 0.05$) and a reduction in G2/M content ($p \leq 0.05$), accompanied by continued suppression of the S phase, consistent with the emergence of a G1-phase arrest phenotype (Figure 1(a) and (b)). Etoposide exposure resulted in further redistribution among the phases, including a decline in the S-phase fraction and an upward shift in G1, although these changes did not reach statistical significance (Figure 1(b)).

After 72 h of continuous exposure, compound **24** induced a marked G1-phase arrest, with G1-phase cells constituting approximately 65% of the population ($p \leq 0.001$) and a concurrent reduction in both S and G2/M fractions ($p \leq 0.001$) (Figure 1(b)). In contrast, ETP treatment produced a robust accumulation of cells in the G2/M phase ($p \leq 0.001$) and a statistically significant depletion of the G1 population

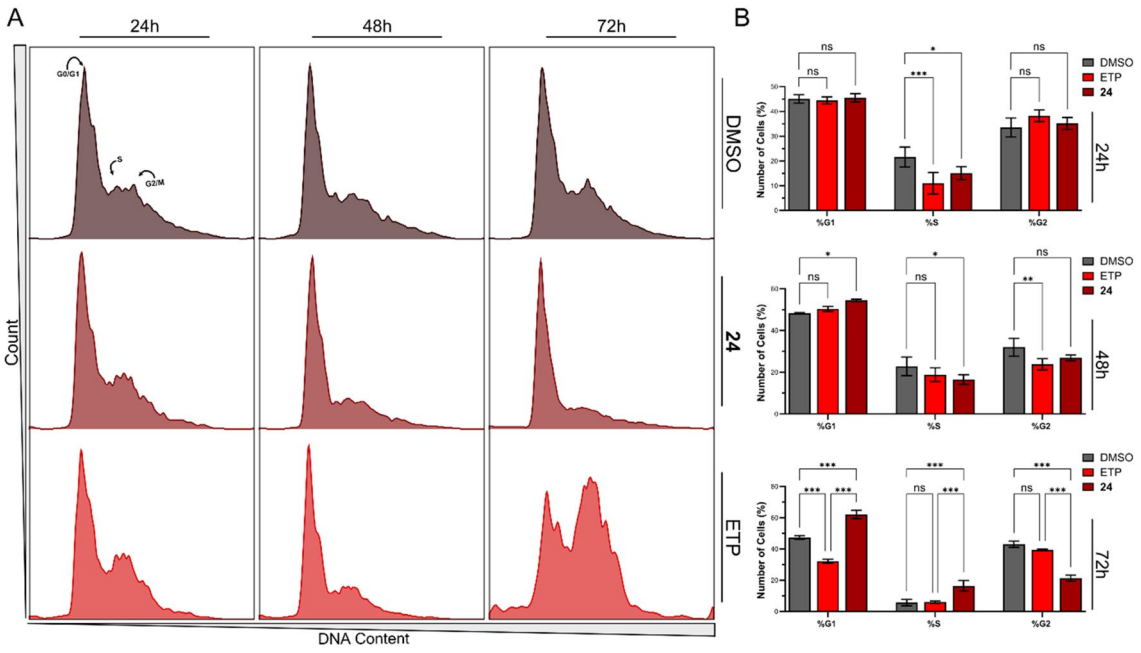

Figure 1. Cell cycle distribution in A-549 cells following treatment with selected compounds for 24 and 48 h at IC_{50} concentrations (a), along with corresponding quantitative analysis (b). Data represent the mean ± SD from three independent biological replicates ($n = 3$). ns $p > 0.05$, *$p < 0.01$, **$p < 0.001$, ***$p < 0.0001$ vs. vehicle (two-way ANOVA and *post hoc* Dunnett's test).

($p \leq 0.001$), corroborating its well-established mechanism of G2/M blockade via topoisomerase II inhibition (Figure 1(b)).

Collectively, these results indicate that compound **24** induces a temporally progressive and statistically robust G1-phase arrest in A-549 cells. These findings warrant further investigation into the molecular pathways underlying **24**-mediated cell cycle regulation and its potential utility as a G1-targeted therapeutic strategy.

Assessment of apoptosis induction in A-549 cells following treatment with compound 24

The pro-apoptotic effects of compound **24** were evaluated in A-549 lung carcinoma cells using two complementary approaches: Annexin V-FITC/7-AAD staining to assess early and late apoptotic events (Figure 2(a) and (b)), and caspase-3/7 activity assays to monitor executioner caspase activation (Figure 2(c) and (d)). ETP was used as a reference pro-apoptotic agent.

Annexin V-FITC/7-AAD staining was performed after 24 and 48 hours of treatment. Cell populations were classified as viable (Annexin V^-/7-AAD^-), early apoptotic (Annexin V^+/7-AAD^-), late apoptotic (Annexin V^+/7-AAD^+), or necrotic (Annexin V^-/7-AAD^+) (Figure 2(a) and (b)). Following 24 hours of exposure to compound **24**, a moderate but statistically significant increase in apoptosis was observed, with early apoptotic cells comprising ~10% and late apoptotic cells ~8% of the population, compared to <4% in vehicle-treated controls (Figure 2(b)). Cell viability remained high (>80%), and necrotic events were negligible (<4%) (Figure 2(b)). ETP induced a markedly stronger apoptotic shift at this time point, increasing early apoptosis to ~25% and decreasing viability to ~65% (Figure 2(b)).

At 48 hours, the divergence between treatments became more apparent. ETP induced a robust apoptotic response, reducing the viable cell population to ~45% and increasing total apoptotic cells (early + late fractions) to ~50% (Figure 2(a)). Compound **24**, meanwhile, produced a moderate but statistically significant increase in apoptosis (early apoptosis ~11%, $p < 0.1$; late apoptosis ~15%, $p < 0.01$), while maintaining approximately 70% cell viability (Figure 2(b)). Necrotic death remained consistently low (<3%) across all treatment conditions, indicating a preference for apoptotic over necrotic mechanisms of cell death (Figure 2(b)).

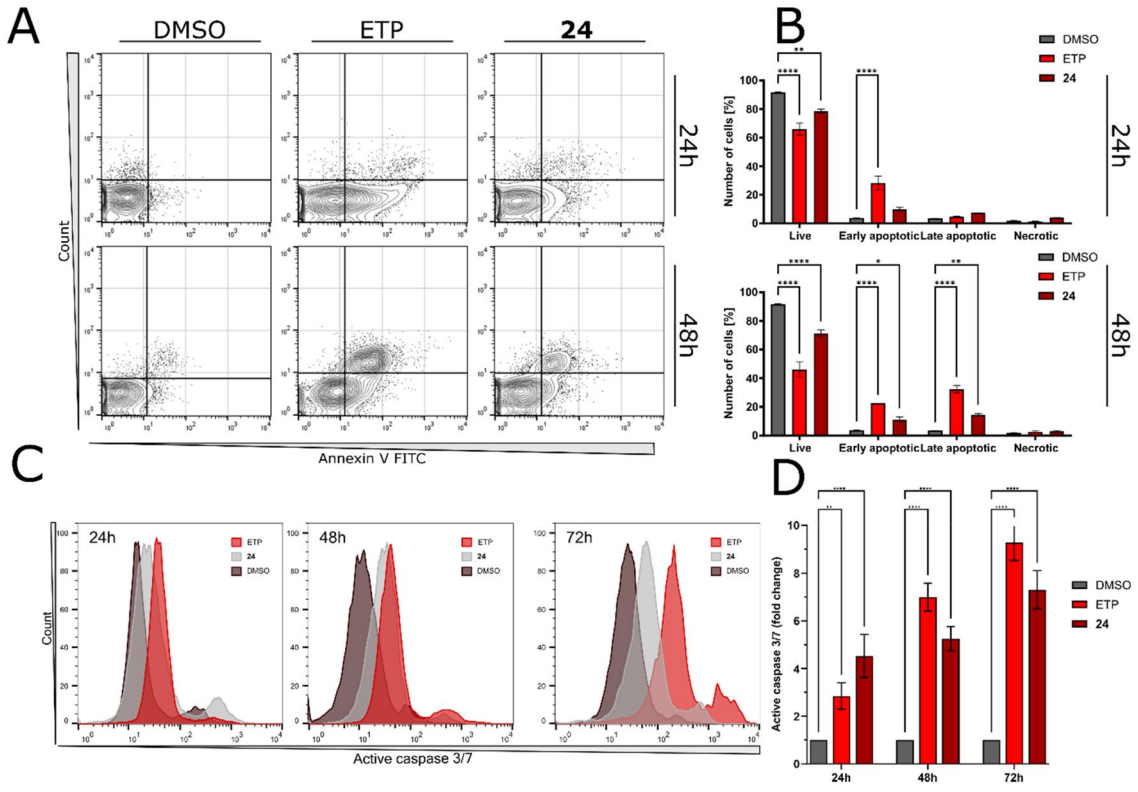

Figure 2. (a) Representative flow cytometry dot plots illustrating Annexin V-FITC and 7-AAD staining of A-549 cells treated with compound **24**, ETP, or DMSO (vehicle) at 24 and 48 h. (b) Quantitative analysis of apoptotic populations presented as mean ± SEM from three independent experiments ($n = 3$). (c) Representative histograms showing caspase-3/7 fluorescence intensity at 24, 48, and 72 h, respectively. (d) Quantitative analysis of caspase-3/7-positive cell populations presented as bar graphs (mean ± SEM, $n = 3$ independent experiments). Statistical significance was determined using two-way ANOVA. *$p < 0.01$, **$p < 0.001$, ***$p < 0.0001$ ****$p < 0.00001$ vs. vehicle (two-way ANOVA and *post hoc* Dunnett's test).

To further capture the progression of apoptosis over time, caspase-3/7 activity was assessed at 24, 48, and 72 hours (Figure 2(c)). This extended timeline was chosen to determine whether caspase activation–often a downstream and sustained event–would continue to intensify beyond the point of phosphatidylserine externalisation detected by Annexin V staining. Compound **24** induced a significant increase in caspase-3/7 activity at 24 hours (~5-fold over control, $p < 0.001$), which remained stable at 48 hours (~5–6 fold), and further rose to ~7-fold at 72 hours ($p < 0.0001$) (Figure 2(d)). ETP showed a delayed but ultimately stronger response: ~3-fold increase at 24 hours, ~7-fold at 48 hours, and ~9–10-fold by 72 hours ($p < 0.0001$ vs. control at all time points; Figure 2(d)).

Together, these findings indicate that compound **24** initiates a caspase-dependent apoptotic program that develops progressively over time while preserving cell viability during early exposure. In contrast, etoposide induces a rapid and extensive apoptotic response, leading to substantial loss of viable cells by 48 hours.

To better understand the upstream events driving this caspase activation, we evaluated whether compound **24** induces oxidative stress or mitochondrial dysfunction—two classical intracellular triggers of apoptosis. Intracellular ROS levels were assessed using the H2DCF-DA assay at 1, 3, 6, and 24 h post-treatment, while mitochondrial membrane potential was analysed using JC-1 staining at 6 and 24 h. In both assays, treatment with **24** did not result in any significant changes compared to DMSO controls (Figures S52 and S53 in Supplementary File 1). No measurable redox imbalance or mitochondrial depolarisation was detected under any of the tested conditions. Flow-cytometric analysis using the DCFH-DA probe showed that compound **24** did not increase intracellular ROS levels relative to vehicle controls across concentrations of 5–30 µM (Figure S53). ROS values remained within ±10% of baseline, with no

statistically significant differences ($p > 0.05$). Similarly, JC-1 staining demonstrated that compound **24** did not reduce mitochondrial membrane potential (ΔΨm) (Figure S52). The red/green fluorescence ratio remained comparable to control levels (90–100% of vehicle), indicating an absence of mitochondrial depolarisation ($p > 0.05$). These findings indicate that compound **24** does not induce a detectable redox imbalance or mitochondrial depolarisation at cytotoxic concentrations. Thus, the observed apoptotic response appears to proceed via non-mitochondrial, caspase-dependent pathways. These data are consistent with the possible involvement of an extrinsic apoptotic component; however, this interpretation remains tentative, as confirmation would require assessment of upstream mediators such as Fas, FADD, and caspase-8.

Evaluation of DNA double-strand break formation in A-549 cells in response to compound 24

To assess the ability of compound **24** to induce DNA damage, we performed a time-course analysis of γH2AX expression using flow cytometry, measuring the percentage of γH2AX-positive cells at 24, 48, and 72 h post-treatment. DNA damage was quantified by p-γH2AX staining in A-549 cells, with DMSO serving as a negative control and ETP as a reference DNA-damaging agent (Figure 3).

At 24 h, compound **24** did not significantly increase γH2AX expression compared to the DMSO control, suggesting minimal early DNA damage (Figure 3(b)). However, a marked elevation in γH2AX-positive cells was observed at 48 h ($p < 0.01$ vs DMSO), indicative of accumulating DNA lesions (Figure 3(b)). Notably, this effect was sustained but not further amplified at 72 h, as the γH2AX levels remained comparable to those measured at 48 h. This plateau suggests that compound **24** triggers a stable DNA damage response that is maintained over time.

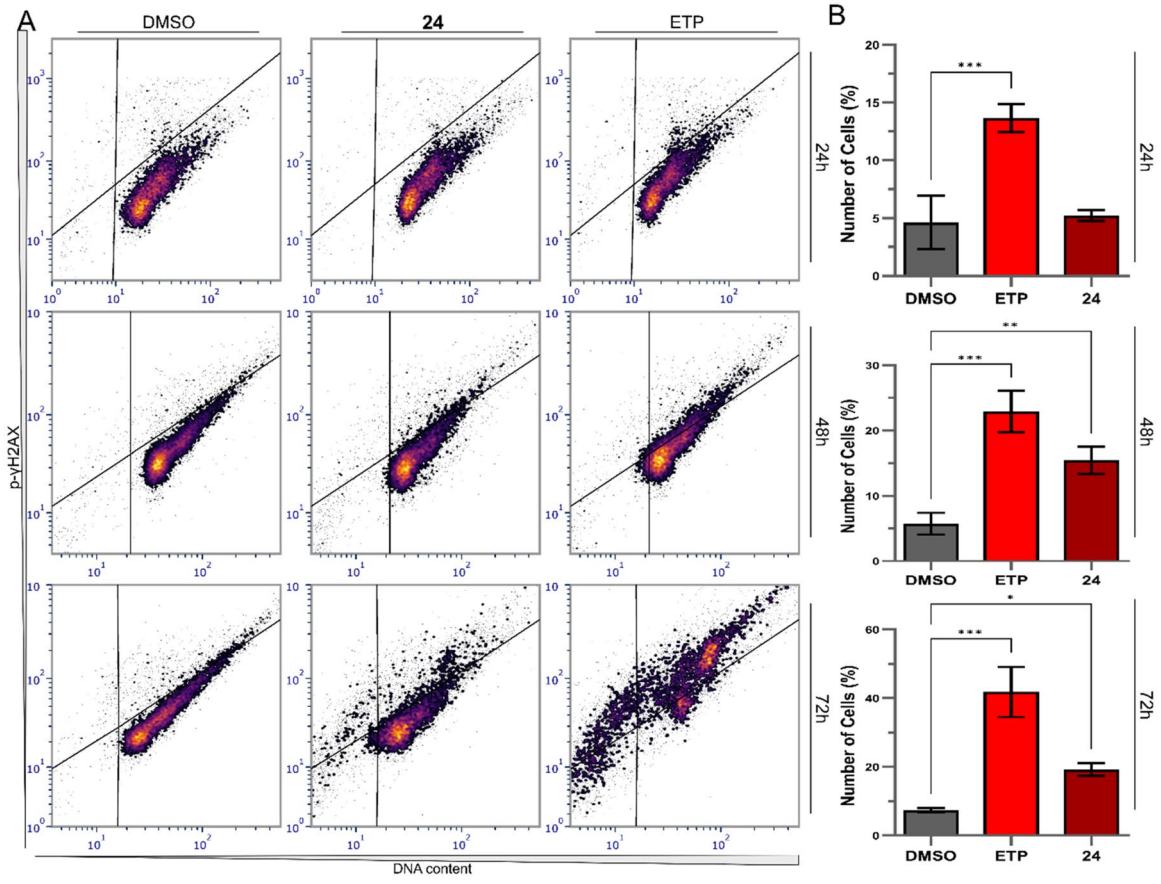

Figure 3. (a) Representative flow cytometry dot plots illustrating p-γH2AX expression in A-549 cells following treatment with compound **24**, ETP, or DMSO (vehicle control) at 24, 48, and 72 h. (b) Quantitative analysis of p-γH2AX-positive cell percentages presented as mean ± SEM from three independent experiments ($n = 3$). *$p < 0.01$, **$p < 0.001$, ***$p < 0.0001$ vs. vehicle (two-way ANOVA and *post hoc* Dunnett's test).

In contrast to ETP, which induced an immediate and robust γH2AX response, compound **24** exhibited a delayed but persistent DNA damage profile, characterised by moderate γH2AX induction (Figure 3(a) and (b)).

The sustained γH2AX signal correlates temporally with previously observed G1-phase arrest at 72 h, implying a mechanistic link between persistent DNA damage and activation of cell cycle checkpoints. These findings suggest that compound **24** induces a controlled DNA damage response that halts cell cycle progression.

Analysis of migration and invasion potential of A-549 cells after treatment with compound 24

To evaluate the anti-migratory potential of compound **24**, a wound healing assay was performed using A-549 cancer cells. Cells treated with the DMSO vehicle control progressively migrated into the wound area over time, leading to near-complete closure by 24 h (Figure 4(a)). Exposure to TGF-β1 further accelerated wound closure, reflecting enhanced migratory behaviour characteristic of an epithelial-to-mesenchymal transition (EMT)-like phenotype (Figure 5(a)).

In contrast, treatment with compound **24** resulted in a significant and concentration-dependent inhibition of cell migration (Figure 4(a)). At all tested concentrations (5, 10, and 15 µM), compound **24** markedly delayed wound closure compared to controls, with the most pronounced differences observed at 24 h (Figure 4(b)). Notably, while a transient reduction in migration was observed between 6 and 12 h at 5 µM, higher concentrations (10 and 15 µM) sustained a persistent wound gap throughout the experiment (Figure 4(b)). At 24 h, the DMSO control showed nearly complete wound closure (~95%), whereas cells treated with 10 or 15 µM compound **24** retained a substantially larger wound area (~30%; $p < 0.001$), corresponding to a ~70% inhibition of migration relative to control. When compound **24** was applied in the presence of TGF-β1, it effectively suppressed the enhanced migratory response, maintaining significant wound areas open even after 24 h (Figure 5(a)). Quantitative analysis corroborated these observations, demonstrating that wound closure reached ~90% after 24 h in the TGF-β1 group, whereas it was limited to ~50% and <30% at 15 µM and 10 µM of compound **24**, respectively (Figure 5(b)). These differences were statistically significant already at 12 h ($p < 0.01$) and even more pronounced at 24 h ($p < 0.0001$; Figure 5(a)). Importantly, no signs of cytotoxicity such as cell detachment were observed during the course of treatment, indicating that the anti-migratory effects of compound **24** were not attributable to cell death.

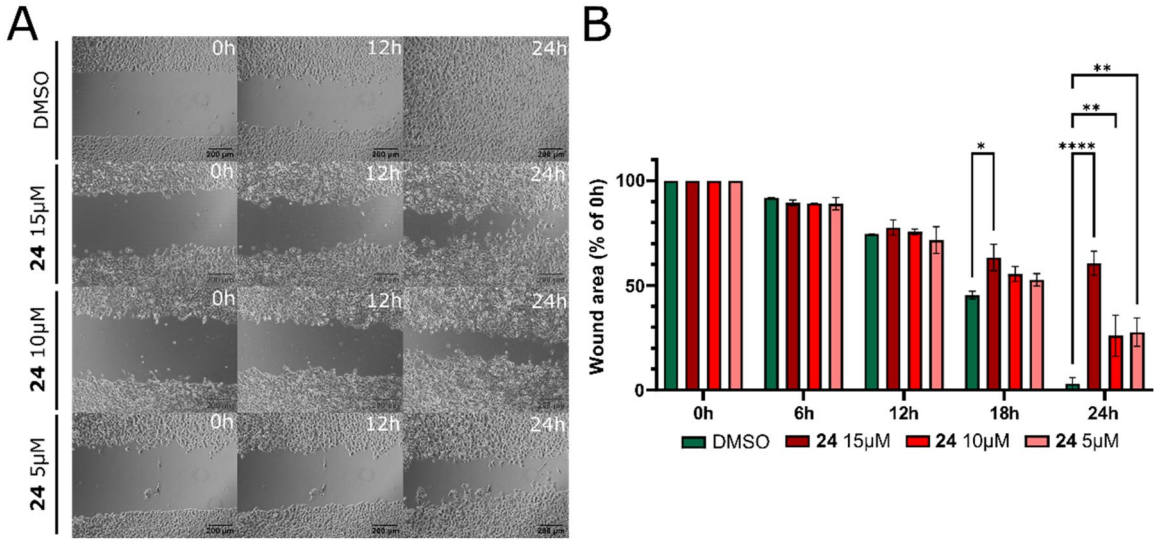

Figure 4. (a) Representative time-lapse microscopy images of A-549 cells after culture insert removal. DMSO was used as a negative control. Scale bars = 200 µm. (b) Quantification of the wound areas after culture insert removal. Data represent the mean ± SEM of three independent experiments.*$p < 0.01$, **$p < 0.001$, ****$p < 0.00001$ vs. vehicle (two-way ANOVA and *post hoc* Dunnett's test).

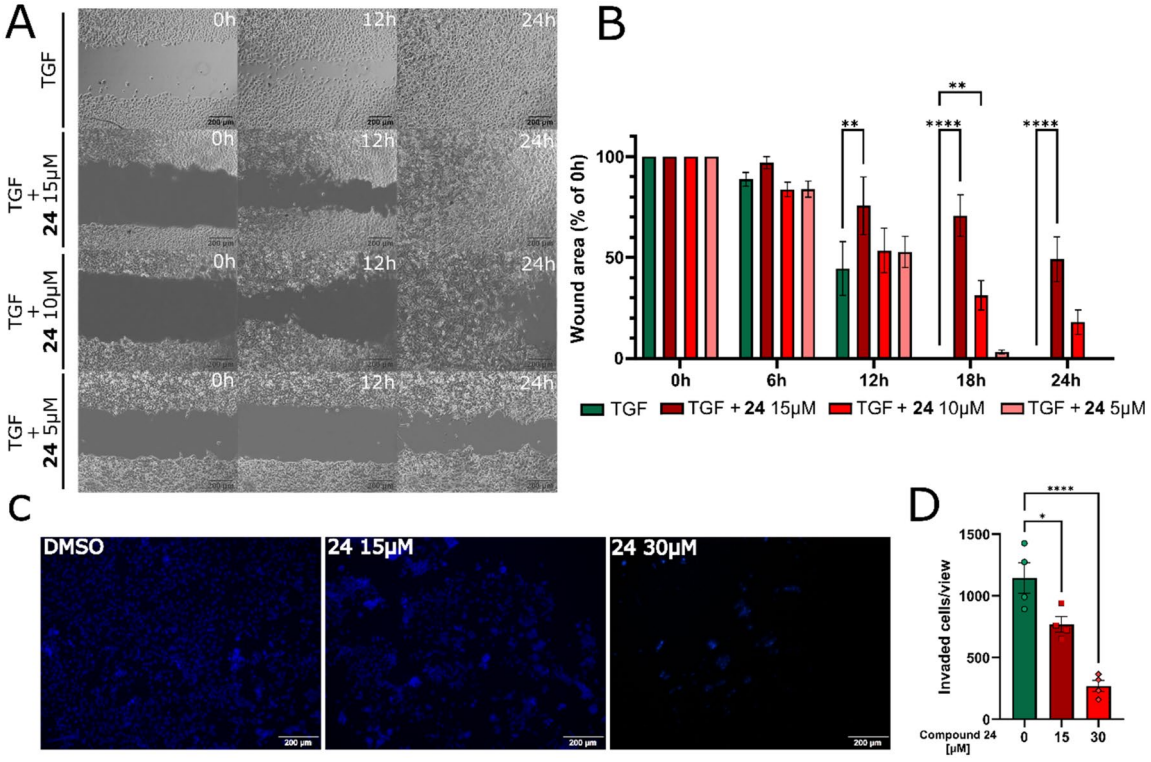

Figure 5. (a) Representative time-lapse microscopy images of A-549 cells after culture insert removal. TGF was used as a negative control. Scale bars = 200 µm. (b) Quantification of the wound areas after culture insert removal. Data were analysed using two-way ANOVA followed by Dunnett's *post hoc* test. (c) Matrigel invasion assay of A-549 cells using a Transwell system. Scale bars = 200 µm. (d) Quantification of invaded cells. All data represent the mean ± SEM of three independent experiments. Data were analysed using one-way ANOVA followed by Dunnett's *post hoc* test. All data represent the mean ± SEM of three independent experiments. * $p < 0.01$, ** $p < 0.001$, *** $p < 0.0001$, **** $p < 0.00001$ vs. vehicle.

To further investigate the anti-invasive properties of compound **24**, a Matrigel-based transwell invasion assay was performed. Fluorescence imaging of DAPI-stained cells that had invaded through the matrix revealed that treatment with compound **24** drastically reduced the number of invading cells (Figure 5(c)). Quantitative analysis confirmed this marked suppression of invasion: at 15 µM, the number of invading cells decreased to ~65% of the TGF-β1 control (≈35% inhibition; $p < 0.01$), while at 30 µM it was reduced further to ~25% of control levels (≈75% inhibition; $p < 0.0001$) (Figure 5(d)).

These data collectively demonstrate that compound **24** potently inhibits both the migration and invasion of A-549 cancer cells. The observed inhibition correlates with the suppression of extracellular matrix degradation and is consistent with a reduction in metastatic potential.

Investigation of MMP2, MMP9, and hTERT expression levels in A-549 cells

Given that matrix metalloproteinases (MMPs) play pivotal roles in extracellular matrix remodelling and metastasis, we next assessed the expression of *MMP2* and *MMP9* after 48 h of treatment. Quantitative real-time PCR analysis revealed a dramatic upregulation of *MMP2* (~10-fold) and *MMP9* (~14-fold) transcripts following TGF-β1 stimulation alone (Figure 6). Treatment with compound **24** at 15 µM significantly suppressed TGF-β1-induced *MMP2* and *MMP9* expression (~60% and ~70% reduction, respectively, $p < 0.01$). At 30 µM, compound **24** almost completely abolished *MMP2* and *MMP9* mRNA levels, reducing them to near baseline or below ($p < 0.0001$). Interestingly, compound **24** also diminished the expression of human telomerase reverse transcriptase (hTERT) (Figure 6), a hallmark of replicative immortality and cancer cell proliferation. *hTERT* expression decreased by ~50% at 15 µM and was almost undetectable at 30 µM ($p < 0.001$). These findings suggest that compound **24** not only impairs invasive behaviour but also affects key elements of tumour cell maintenance and survival.

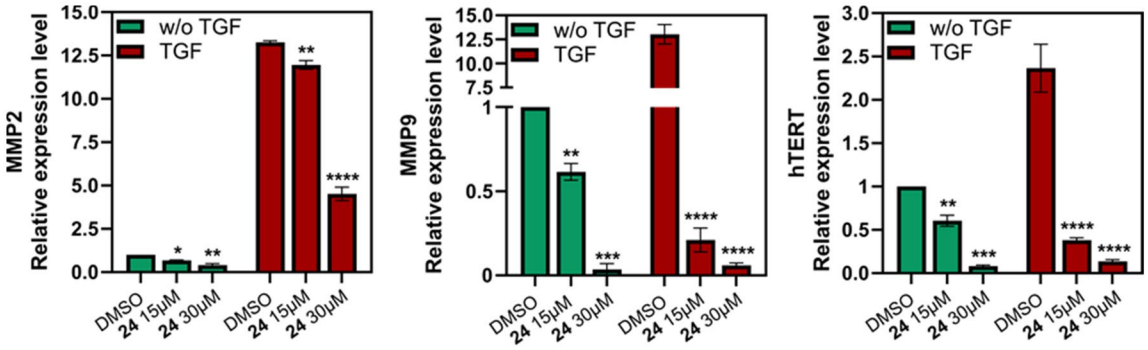

Figure 6. RT-PCR analyses of *MMP2*, *MMP9* and *hTERT* mRNA expression in A-549 cells after treatment with **24** for 48 h. Expression was normalised to RNA polymerase subunit (*RPII*). Error bars represent the SEM of data obtained in $n = 3$ independent experiments. *$p < 0.01$, **$p < 0.001$, ***$p < 0.0001$, ****$p < 0.00001$ vs. vehicle (two-way ANOVA and *post hoc* Dunnett's test).

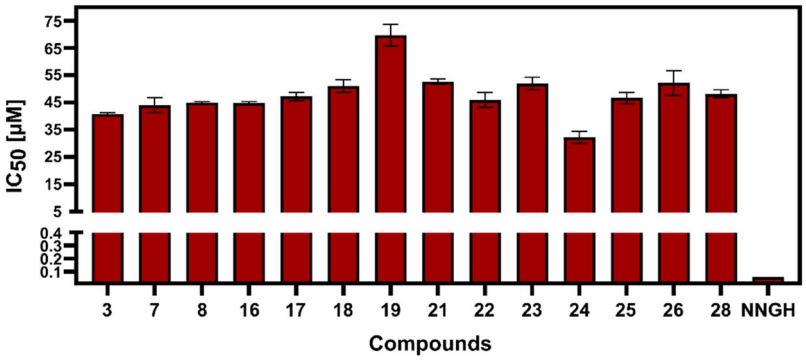

Figure 7. Inhibitory activity of selected S-substituted imidazole-2-thione derivatives against MMP-9. Bars represent IC_{50} values calculated from three independent experiments (mean ± SD).

Inhibition of MMP-9 activity

All compounds that exhibited cytotoxicity in the MTT assay were further evaluated for their inhibitory potential against MMP-9. The analysis was restricted to MMP-9, as RT-qPCR experiments indicated that compound **24** produced a stronger reduction in *MMP-9* gene expression compared to *MMP-2*.

The tested imidazole-2-thione derivatives demonstrated inhibitory activity towards MMP-9 with half-maximal inhibitory concentration (IC_{50}) values ranging from 34.46 to 65.65 µM (Figure 7). Among the evaluated compounds, the most potent inhibitor was compound **24** (IC_{50} = 34.46 µM). Compounds **3** (40.32 µM), **25** (44.65 µM), **16** and **8** (45.21 µM each), and **17** (45.65 µM) also showed moderate activity. By contrast, compound **19** was the weakest inhibitor with an IC_{50} of 65.65 µM. For reference, the prototypic inhibitor NNGH displayed an IC_{50} of 60.56 nM, validating the assay conditions and underscoring the substantially higher potency of the control compared to the tested derivatives.

Examination of three-dimensional spheroid expansion in A-549 cells

In a three-dimensional spheroid-growth assay, we monitored the projected area of A-549 spheroids over 72 h following treatment with compound **24** at concentrations of 10, 25, or 50 µM, using DMSO as the vehicle control (Figure 8(a)). Immediately after medium replacement, all spheroids exhibited a transient contraction to less than 15% of their initial area, likely due to mechanical stress unrelated to compound activity. In the control group, spheroids gradually regained volume, reaching approximately 45% of the baseline area by 24 h and continuing to increase steadily, eventually plateauing at 80–90% between 48 and 72 h (Figure 8(b)). In contrast, treatment with compound **24** significantly delayed spheroid regrowth and limited their expansion in a concentration-dependent manner (Figure 8(a)). At 24 h, spheroid areas reached 33 ± 4% (10 M), 31 ± 3% (25 µM), and 28 ± 3% (50 µM), corresponding to a 26–38% reduction

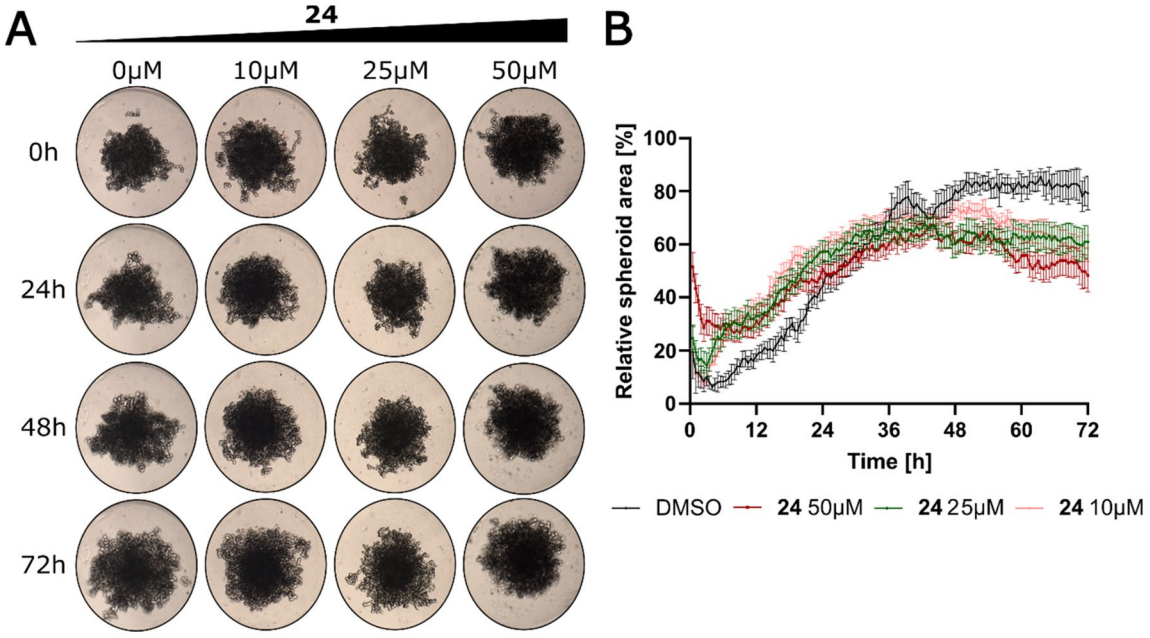

Figure 8. Compound **24** impairs the expansion of A-549 spheroids in a three-dimensional culture model. (a) Representative bright-field images of A-549 spheroids captured at selected time points over a 72-h period following treatment with vehicle (DMSO) or compound **24** at concentrations of 10 µM, 25 µM, or 50 µM. Images show the projected area of individual spheroids, with a visible inhibition of spheroid expansion in a dose-dependent manner. (b) Quantification of spheroid area over time expressed as a percentage of initial size. Values represent the mean ± SEM of $n = 30$ spheroids per condition.

compared to DMSO-treated cultures (two-way ANOVA with Dunnett's post-test, $p < 0.01$). This inhibitory effect was sustained throughout the duration of the assay: spheroids treated with 10 or 25 µM stabilised at approximately 68% and 64% of the initial area, respectively, while those exposed to 50 µM reached a maximum of ~60% at 36 h, followed by a gradual decline to 52 ± 5% at 72 h, indicating a durable ~35% suppression relative to control. Importantly, no cell detachment or visible disintegration of the spheroid structure were observed at any concentration, suggesting that the reduced expansion is not a consequence of acute cytotoxicity but rather reflects impaired collective cell migration and/or proliferation. These findings corroborate two-dimensional wound-healing data and support the antimigratory activity of compound **24** in a physiologically relevant three-dimensional context.

Evaluation of tumour growth and invasive behaviour in the CAM model

Fertilised chicken eggs were maintained *in ovo* throughout the experimental period. On embryonic day 10 (EDD10), A-549 cells pre-labelled with CellTracker™ Green CMFDA were carefully applied onto the chorioallantoic membrane (CAM) surface and allowed to grow for five days. Following tumour implantation, compound **24** was administered topically at final concentrations of 25 µM or 50 µM, whereas the control group received an equivalent volume of vehicle (DMSO). Treatment continued for 48 h, after which the CAMs were harvested for imaging.

Tumour growth and morphology were monitored using both bright-field stereomicroscopy and fluorescence microscopy under identical exposure settings (Figure 9). In vehicle-treated controls, A-549 xenografts showed robust expansion, forming opaque and sharply demarcated nodules associated with a dense, radially organised vascular network (Figure 9(a)). In contrast, treatment with compound **24** significantly limited tumour expansion in a dose-dependent manner. A 25 µM dose reduced the median area to 0.02 ± 0.001 mm^2 (77% of control), while 50 µM further decreased it to 0.017 ± 0.001 mm^2 (62% of control; $p < 0.01$, one-way ANOVA with Dunnett's *post hoc* test; Figure 9(b)).

Consistent with macroscopic observations, fluorescence microscopy revealed strong, well-defined CellTrackerGreen signals in control tumours, indicative of high cellular viability and density (Figure 9(c)). Conversely, tumours treated with **24** exhibited markedly weaker and less homogeneous fluorescence, suggesting a reduction in tumour cell viability and/or cellular density. Notably, there were no signs of

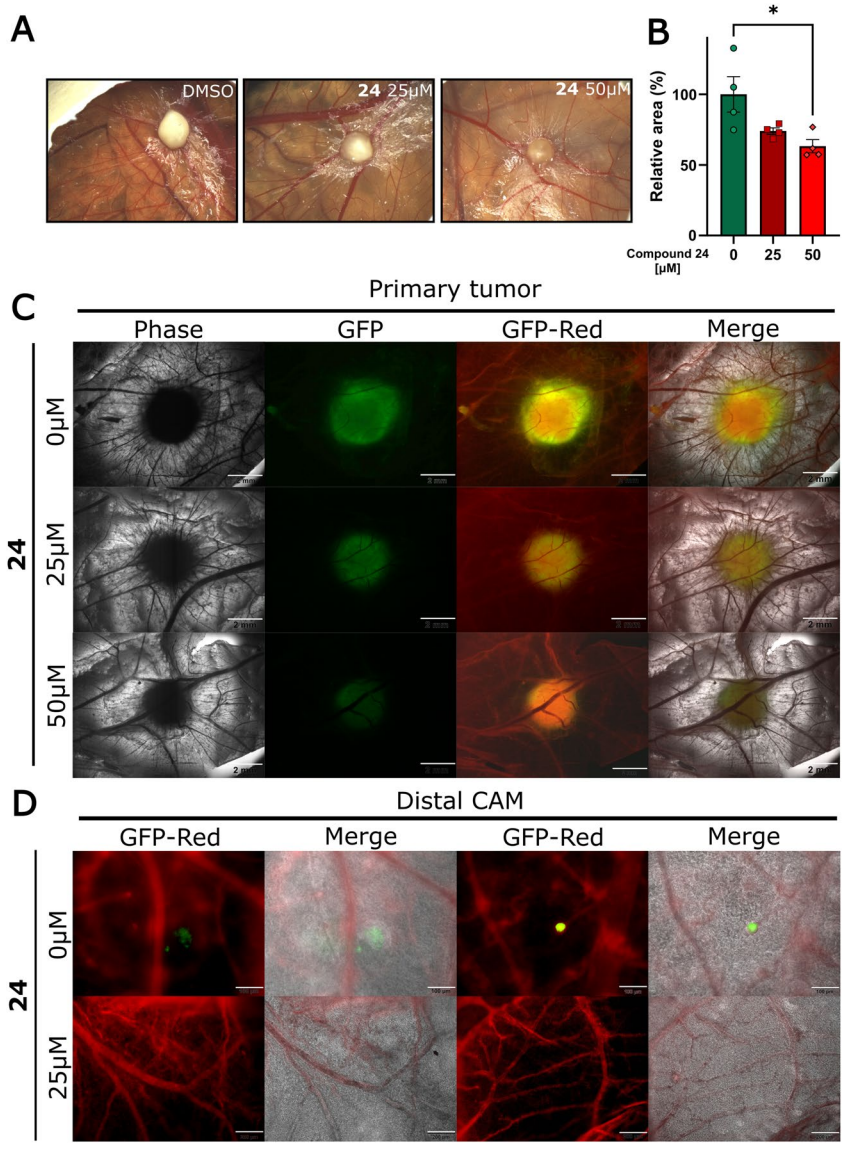

Figure 9. (a) Representative images of the chorioallantoic membrane (CAM) on embryonic day 17, corresponding to the endpoint of the experimental procedure. (b) Quantification of microtumor-covered area relative to the analysed CAM region, performed using ImageJ software. Data represent $n = 5–7$ tumours from 7 embryos per group. *$p < 0.01$ (one-way ANOVA, Dunnett's test). (c) Fluorescence microscopy of A-549-derived tumours developed on the CAM following 48-h treatment with compound **24** or vehicle control (0.5% v/v DMSO in PBS). Viable tumour cells are shown in green (CellTracker Green), and angiogenic vasculature is visualised in red using rhodamine-conjugated LCA. Scale bar: 2 mm. (d) Vasculotropic behaviour of A-549 cells, indicated by their migration from the primary tumour site and extravasation into distant regions of the CAM. Scale bars: 200 µm (vehicle – 0 µm) and 100 µm (compound **24**).

haemorrhage, necrosis, or graft detachment in either group, indicating that the inhibitory effects were not due to overt toxicity to the embryo (Figure 9(a) and 9(c)).

Importantly, high-magnification imaging revealed significant differences in the vasculotropic behaviour of A-549 cells (Figure 9(d)). In the control group, green-fluorescent tumour cells were frequently observed migrating away from the primary graft site and extravasating into distal areas of the CAM, indicating active dissemination. In stark contrast, embryos treated with **24** showed a near-complete absence of disseminated fluorescent cells beyond the tumour mass. This observation suggests that compound **24** effectively inhibits not only primary tumour expansion but also the migratory and invasive potential of A-549 cells, thereby preventing distal colonisation of the CAM. Together, these findings highlight the dual inhibitory effect of compound **24** on tumour proliferation and cellular dissemination under physiologically relevant conditions, without inducing systemic toxicity in the developing embryo.

In silico evaluation

Molecular docking studies were performed on MMP-2 and MMP-9 using all proposed compounds (Table S1 in Supplementary File 1). However, subsequent *in silico* calculations and experimental validations were focused exclusively on compound **24**, which demonstrated the highest activity in preliminary *in vitro* assays. For docking, the co-crystallized ligands were extracted from the active sites of the crystal structures, and redocking was conducted using the parameters detailed in the Methods section. The docked ligand **24** was found to occupy the active sites of both MMP-2 and MMP-9 with high fidelity (Figure 10(a)). Molecular dynamics (MD) simulations were carried out for 500 ns to assess the stability of the protein–ligand complexes. The RMSD analysis indicated minimal structural fluctuations in both MMP-2 and MMP-9 when complexed with **24**, suggesting that the ligand remains stably bound in the active site

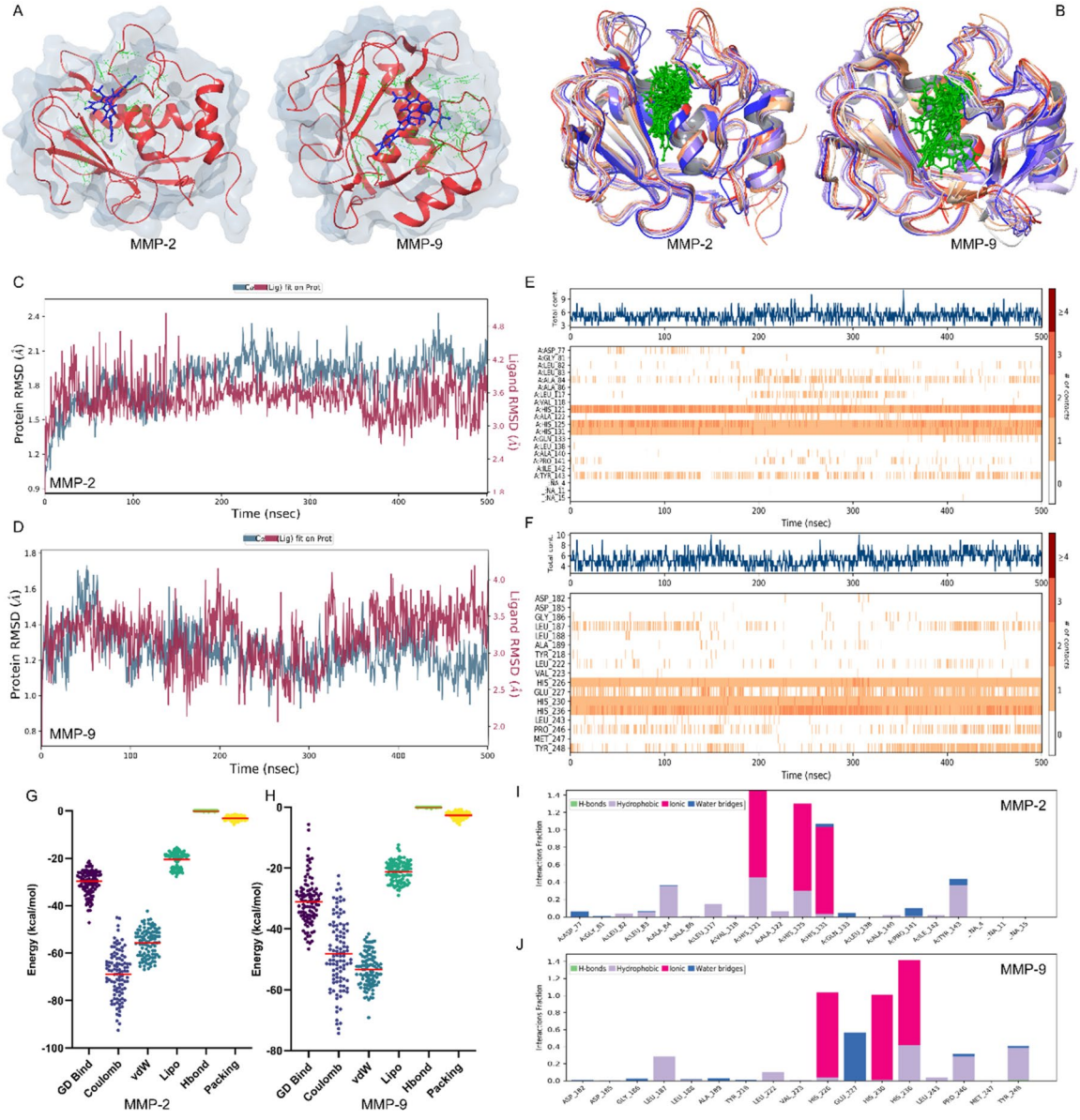

Figure 10. Binding pose of compound **24** on MMP2 and 9 (a), position of compound **24** on 10 snapshots from 500 ns MDrun (b). RMSD of ligand and protein (c) MMP2 (d) MMP9. A timeline representation of the interactions of (e) MMP2 (f) MMP9 shows which residues interact with the ligand in each trajectory frame. Some residues make more than one specific contact with the ligand, which is represented by a darker shade of orange. The contributions of various energy components to the total binding energy of the drug-Protein complexes (g) MMP2 (h) MMP9. Representation of the interactions and contacts (H-bonds, Hydrophobic, Ionic, Water bridges) of (i) MMP2 (j) MMP9.

Table 3. The contributions of various energy components to the total binding energy of the drug-Protein complexes after the MD run*.

Name	Average Binding Energy (kcal/mol)	Coulomb	vdW	Lipo	Hbond	Packing
MMP2	−30.47 ± 5.07	−68.90 ± 4.94	−55.73 ± 5.88	−20.56 ± 3.38	−0.02 ± 0.07	−3.71 ± 0.94
MMP9	−30.88 ± 7.69	−48.15 ± 1.64	−53.25 ± 5.25	−21.09 ± 3.29	−0.09 ± 0.04	−2.68 ± 1.13

*Coulomb – Coulomb energy, vdW – Van der Waals energy, Lipo – Lipophilic energy, Hbond – Hydrogen bonding correction, Packing – pi-pi packing correction.

throughout the simulation period (Figure 10(c) and (d)). Key interacting residues identified in MMP-2 during the simulation include His121, His125, and His131, while His226, His230, and His236 were found to be prominent in MMP-9 (Figure 10(e)–(f)). The positional stability of molecule **24** throughout the simulation is further visualised by overlaying the ligand conformations sampled every 100 frames (10 frames per snapshot from a total of 1000 frames), as shown in Figure 10(b).

The MM-GBSA (Molecular Mechanics/Generalized Born Surface Area) calculations performed on compound **24** in complex with MMP9 and MMP2 over 100 evenly spaced frames from independent 500 ns MD simulations revealed comparable overall binding free energies. For MMP9, the average binding free energy (ΔG_bind) was −30.98 ± 7.72 kcal/mol, while for MMP2 it was slightly less favourable at −30.43 ± 5.07 kcal/mol. Despite their close numerical proximity, notable differences in energetic contributions were observed, suggesting distinct binding mode characteristics between the two metalloproteinases. In both complexes, Coulombic interactions emerged as the dominant favourable component, although their magnitude differed substantially. MMP2 exhibited a markedly stronger Coulombic stabilisation (–68.88 ± 9.90 kcal/mol) compared to MMP9 (–48.21 ± 11.60 kcal/mol). However, this gain was offset by a significantly higher solvation penalty in MMP2 (+111.86 ± 9.93 kcal/mol) compared to MMP9 (+90.64 ± 11.65 kcal/mol), possibly reflecting the stronger desolvation cost due to tighter or more polar binding in the former (Figure 10(g) and (h)). The lipophilic (hydrophobic) contributions were similar across both targets, averaging −20.55 kcal/mol in MMP2 and −21.16 kcal/mol in MMP9, highlighting the consistent role of hydrophobic contacts in stabilising the ligand. Hydrogen bonding was minimal in both cases, with negligible mean values close to zero (–0.02 kcal/mol for MMP2, −0.013 kcal/mol for MMP9). Interestingly, covalent strain energy was notably higher in MMP2 (+6.09 ± 5.27 kcal/mol) than in MMP9 (+3.87 ± 2.89 kcal/mol), possibly indicating increased conformational strain or less optimal geometry upon binding in the MMP2 active site. Packing (van der Waals) interactions were slightly more stabilising in MMP9 (–2.69 kcal/mol) compared to MMP2 (–3.18 kcal/mol), though both were modest in magnitude (Table 3). In summary, compound **24** binds stably to both MMP-2 and MMP-9 with comparable affinity but via distinct energetic balances—MMP-2 binding being more electrostatically driven yet more strongly penalised by solvation, whereas MMP-9 shows a more balanced contribution of hydrophobic and Coulombic interactions.

Discussion

The present study provides a comprehensive pharmacological characterisation of newly synthesised imidazole-2-thione derivatives, highlighting compound **24** as a lead structure with both cytotoxic and anti-metastatic activity. Notably, while other analogues in this series (e.g. compounds **23** and **26**) also showed appreciable anticancer activity, compound **24** emerged as the lead due to its superior balance of potency, selectivity, and anti-metastatic efficacy. The 4-chloro substitution in compound **24**'s phenyl rings may impart an optimal combination of physicochemical properties—such as increased lipophilicity, a favourable binding conformation for MMP active sites, and possibly enhanced metabolic stability—contributing to its enhanced performance relative to the mono-substituted analogues. The data presented here indicate that the compound exerts its effects through multiple, complementary mechanisms, which together may offer advantages over single-target anticancer drugs.

Compound **24** demonstrated submicromolar to low micromolar IC_{50} values in several human cancer cell lines, most prominently A-549 lung adenocarcinoma. Flow cytometry analysis of DNA content revealed an accumulation of cells in the G0/G1 phase, with a corresponding reduction in S-phase population, indicating that **24** halts cell cycle progression prior to DNA replication. This G1 arrest could reflect interference with cyclin D/E–cdk4/2 signalling or activation of cell cycle checkpoints in response to

cellular stress.[27,28] Indeed, evidence of DNA damage was observed in compound **24**-treated cells, as indicated by markers such as p-γH2AX foci. The DNA damage likely triggers the G1/S checkpoint (via p53/p21 or other pathways), contributing to cell cycle blockade.[29,30] Many classical cytotoxic drugs (e.g. doxorubicin or etoposide) induce DNA damage and arrest cells in G2/M or S phase, whereas the G1-phase arrest by compound **24** suggests a possibly different primary mechanism.

Importantly, several canonical mechanisms of DNA injury can be reasonably excluded. Etoposide, a prototypical topoisomerase II inhibitor, induces an immediate and robust γH2AX response together with strong G2/M accumulation and extensive apoptosis. In contrast, compound **24** produces a delayed and sustained γH2AX signal, progressive G1 arrest, and only moderate apoptosis—a phenotype incompatible with topo-like activity. Consistently, imidazole-2-thione scaffolds have not been reported as topoisomerase inhibitors. Direct DNA intercalation is also unlikely. Classical intercalators such as doxorubicin or mitoxantrone induce pronounced S-phase arrest, rapid apoptosis, and require extended planar aromatic systems absent from compound **24**. We initially considered whether oxidative stress might be involved; however, our measurements showed that compound **24** did not induce ROS production or mitochondrial depolarisation in treated cells, indicating that the G_1 arrest is not attributable to a redox-mediated mechanism. Taken together, these observations suggest that compound **24** induces DNA damage through non-classical routes and therefore alternative mechanisms should be considered. These may include nucleotide pool depletion, replication-fork slowing or stalling at the onset of S-phase, or transcription–replication conflicts that generate localised γH2AX accumulation. In this scenario, compound **24** would trigger an early replication-stress response—potentially involving nucleolar or transcriptional perturbations—that activates G1/S checkpoints without the features typical of topoisomerase poisons or classical intercalators.[31,32] Importantly, the DNA damage response elicited by compound **24** appears to function as a critical pro-death signal that amplifies its antiproliferative activity. Nonetheless, the precise origin and molecular nature of the DNA damage remain to be elucidated in future mechanistic studies. Consistent with its ability to damage DNA and disrupt the cell cycle, compound **24** effectively triggered apoptosis in cancer cells. Treated cell populations showed a significant increase in apoptotic indicators (e.g. phosphatidylserine externalisation and caspase-3 cleavage), confirming that cell death occurred via programmed apoptotic pathways rather than necrosis. The induction of apoptosis is a desirable attribute in an anticancer agent, as it facilitates orderly cell elimination and reduces the risk of triggering inflammation in the tumour microenvironment.[33,34] Notably, compound **24** induced apoptosis in a dose-dependent manner, and importantly, it achieved substantial apoptosis in cancer cells at concentrations that caused only minimal toxicity in non-malignant cells. This indicates a degree of selectivity for tumour cells, possibly due to cancer-specific uptake or vulnerability, and results in a favourable selectivity index. In our experiments, compound **24** was noticeably less toxic to normal fibroblasts than to multiple cancer cell lines, with selectivity index of approximately 4. While MRC-5 is a widely used and accepted comparator in cytotoxicity studies, a broader panel of adult human normal cells—such as primary hepatocytes or renal epithelial cells—will be required to validate and refine the selectivity of compound **24**. Although further studies are needed to fully ascertain safety, this selectivity suggests that compound **24**'s mechanism exploits vulnerabilities unique to cancer cells (such as their higher basal oxidative stress or reliance on certain survival pathways), thereby sparing normal cells to a greater extent. Many conventional chemotherapeutics have only narrow therapeutic windows, so the apparent selectivity of **24** is encouraging for its potential as a lead compound.[35]

In parallel to its cytotoxic effects, compound **24** demonstrated robust anti-metastatic activity *in vitro*. In wound-healing (2D migration) assays, treated cancer cell monolayers exhibited significantly delayed wound closure, indicating impaired migratory capacity. More strikingly, in Boyden chamber invasion assays, compound **24** dramatically reduced the number of cells invading through the Matrigel-coated membrane compared to controls. This anti-invasive effect was observed at sublethal doses that minimally affected cell viability, suggesting that **24** specifically impairs cancer cells motility and invasiveness rather than eliminating cells before they can migrate. Such activity is particularly valuable because metastasis is poorly addressed by most cytotoxic drugs – in fact, the standard chemotherapies that target proliferating cells often fail to prevent the migration of surviving cells, and in some cases sublethal chemotherapy stress may paradoxically enhance migratory phenotype.[3,36,37] By contrast, compound **24** appears to

actively counteract the processes of migration and invasion. The net result is a compound that not only reduces the tumour cell population but also restrains the invasive behaviour of the residual fraction, potentially limiting metastatic spread. This kind of dual typically requires combination therapy (e.g. using a cytotoxic agent alongside a separate anti-metastatic inhibitor), so it is notable that compound **24** delivers both effects in a single molecular entity.[38]

The anti-metastatic efficacy of compound **24** was further evidenced in 3D tumour spheroid models and the CAM embryo model, which more closely mimic the tumour microenvironment and metastatic process.[39,40] In 3D spheroid culture, compound **24**-treated tumour spheroids displayed limited outgrowth: their size remained small and viable cell density was greatly reduced relative to untreated spheroids. Treated spheroids often showed dark, necrotic or apoptotic cores and failed to invade into the surrounding matrix, whereas control spheroids expanded and infiltrated the matrix over time.[41] This indicates that compound **24** can penetrate a 3D cell mass and inhibit not only cell proliferation inside spheroids but also the collective invasion of cells from the spheroid periphery. Importantly, *in vivo* testing using the chick CAM model corroborated these findings, as tumour cells grafted onto the CAM and exposed to compound **24** formed significantly smaller tumour masses. Although the CAM model has limitations (e.g. it is an embryonic model and lacks an adaptive immune system), it provides a convenient *in vivo*-like system to observe metastasis-related phenomena such as local invasion and intravasation.[39,42,43] The positive results in this model strengthen the case that compound **24**'s anti-metastatic effects are not an artefact of *in vitro* systems but do translate into a living organism context. Nevertheless, because of these limitations, further evaluation in mammalian models is warranted. To address this, follow-up studies in immunocompetent murine xenograft and metastatic models are planned as the next stage of preclinical validation, allowing assessment of compound **24** in a more physiologically relevant environment that includes interactions with the immune system.

The pronounced cytotoxic and anti-metastatic effects of compound **24** prompted us to investigate its underlying molecular targets and mechanisms of action. The design of our imidazole-2-thione derivatives was initially influenced by the known role of matrix metalloproteinases (MMPs) in cancer invasion and metastasis.[5] The imidazole-2-thione core, especially with appropriate substituents, can serve as a zinc-binding group, theoretically enabling inhibition of Zn-dependent enzymes like MMPs. Molecular docking studies performed on MMP-2 and MMP-9 active sites, indicated that compound **24** is indeed capable of coordinating the catalytic Zn^{2+} ion via its thione sulphur and forming additional contacts in the hydrophobic-binding pocket (mimicking the binding mode of known MMP inhibitors). This prediction was validated experimentally for MMP-9: enzymatic assays demonstrated inhibition with an IC_{50} of 34 µM. Although weaker than classical hydroxamate-based inhibitors such as NNGH, which act in the nanomolar range, this finding nonetheless confirms that **24** directly targets MMP-9. Importantly, enzymatic inhibition correlated with reduced *MMP-9* mRNA expression in treated cells, indicating that **24** exerts a dual effect by blocking enzyme activity and suppressing its production. This combination provides a partial but plausible explanation for the pronounced impairment of cancer cell migration and invasion observed in functional assays.

When placed in the context of prior MMP inhibitor research, the significance of these findings becomes clearer. More than 50 small-molecule MMP inhibitors, many with nanomolar potency, failed in clinical trials due to severe musculoskeletal toxicity, lack of selectivity, and redundancy within the protease network.[44] Moreover, direct MMP inhibition by small molecules often lacked selectivity (many MMPs share homologous active sites) and led to dose-limiting side effects, undermining their clinical tractability.[44] In contrast, compound **24**, despite its only micromolar potency against MMP-9, combines moderate enzymatic inhibition with suppression of expression and additional cytotoxic and anti-metastatic mechanisms. This broader, polypharmacological activity may explain why its biological effects are more pronounced than would be expected from enzymatic potency alone, and why it may overcome some of the limitations that hindered earlier generations of MMP-targeted drugs.

Beyond its effects on MMPs, compound **24** was also found to downregulate telomerase (hTERT), the enzyme responsible for maintaining telomere length and a hallmark of cellular immortality in cancer. Suppression of *hTERT* expression may further limit the long-term proliferative capacity of cancer cells, thereby complementing the immediate cytotoxic effects of the compound.[45] Importantly, emerging

evidence indicates that hTERT contributes not only to telomere maintenance but also to metastatic progression, as it can upregulate genes involved in migration and invasion and has been correlated with enhanced metastatic behaviour independent of its canonical telomere-related role.[46–48] Thus, the decrease in *hTERT* expression observed in compound **24**-treated cells provides an additional mechanistic explanation for its anti-metastatic activity. In combination with MMP-9 inhibition and reduced enzyme expression, *hTERT* downregulation suggests that compound **24** interferes with multiple hallmarks of cancer simultaneously – targeting both invasiveness and replicative immortality while directly inducing cell death. However, the current data do not allow us to determine whether hTERT downregulation reflects a direct action of compound **24** or arises secondarily from broader cellular stress such as G1 arrest or DNA damage. These stress responses are known to influence hTERT transcription via key promoter regulators including c-Myc and Sp1, raising the possibility that the observed effect may be indirect.[49] Clarifying this will require targeted promoter-level analyses—such as measuring hTERT promoter activity and evaluating c-Myc/Sp1 expression and binding—to distinguish between primary and secondary mechanisms. Such mechanistic resolution is essential for defining how compound **24** engages the telomerase regulatory network. Overall, this multi-pathway impact aligns with a polypharmacological mode of action, where modest modulation of several pathways yields an additive or synergistic effect on the malignant phenotype.

It is also noteworthy that, despite the presence of a reactive sulphur group in its structure, compound **24** did not exhibit obvious redox-related side effects.[50,51] Certain imidazole-2-thione derivatives, such as PX-12, are known to perturb the cellular redox balance and increase oxidative stress, but we observed no ROS accumulation in compound **24**-treated cells.[52] These findings argue against non-specific oxidative cytotoxicity as the main mode of action. While covalent interactions with protein thiols cannot be completely excluded without targeted studies, the absence of classical redox-associated toxicity, together with the selective phenotypic profile we observed, suggests a more specific and multi-targeted mechanism of action for compound **24**.

We also emphasise the contrast with structurally related compound **28**, which exhibited pronounced toxicity towards MRC-5 fibroblasts (SI = 0.35). In comparison, compound **24** showed a markedly improved selectivity index (~4) and no overt toxicity in the CAM assay, with no signs of haemorrhage, embryo lethality, or vascular damage. Although systemic acute toxicity assays (e.g. haemolysis, hepatocyte viability) and genotoxicity tests (e.g. Ames, micronucleus) have not yet been performed, these evaluations are part of our planned preclinical pipeline. Importantly, the absence of ROS induction, stable mitochondrial membrane potential, and selective activity *in vitro* and *in ovo* all argue against non-specific redox or genotoxic liabilities for compound **24**, although comprehensive systemic toxicity and genotoxicity studies remain necessary to firmly establish its safety profile.

Comparing compound **24**'s profile to existing therapies, we find that it combines features typically seen in separate drug classes. Classical cytotoxic chemotherapeutics like doxorubicin or paclitaxel are highly potent at killing tumour cells and can induce apoptosis, but they generally do not specifically inhibit metastasis (and any remaining invasive cells can continue to spread).[53,54] Conversely, dedicated anti-metastatic agents (such as MMP inhibitors or integrin blockers) can impede invasion but usually lack tumoricidal power and have failed to show clinical benefits when used alone.[44] Compound **24** bridges this gap by simultaneously exerting both effects: it substantially reduces tumour cell viability and independently suppresses invasive behaviour. In principle, a drug with this dual cytotoxic and anti-metastatic activity could provide a two-pronged therapeutic benefit – essentially a single-agent combination therapy. This approach might simplify treatment regimens and reduce the need for multiple drugs, which is advantageous considering that combination therapies often increase toxicity and introduce pharmacokinetic interactions.[55] Moreover, by targeting multiple pathways at once, such an agent could make it more difficult for cancer cells to develop resistance. Tumours often evade single-agent therapies by activating alternate pathways or undergoing phenotypic changes; a multi-target approach like that of compound **24** means that even if a cell manages to resist the cytotoxic insult, it may still be hampered in other critical functions (migration, invasion, etc.).[5] Indeed, multi-target or polypharmacological agents are increasingly acknowledged for their potential to more effectively address complex diseases such as cancer, compared to highly selective compounds.[5]

Conclusion

The synthesis of new S-substituted imidazole derivatives **6–30** with good to excellent yields of 74–98% was carried out through the interaction of thioxoimidazoles **1–5** with methyl 2-bromoacetate (for **6–10**), 1-chloropropan-2-one (for **16–20**) or the corresponding bromoacetophenone (for **21–30**). Among these compounds, our biological findings highlight compound **24** as a compelling lead in the development of multifunctional anticancer agents. This derivative combines potent cytotoxic mechanisms—G1 cell cycle arrest, DNA damage, and apoptosis induction—with robust anti-metastatic actions, including inhibition of migration, invasion, and spheroid outgrowth, as well as suppression of tumour growth and vasculotropic spread in the CAM model.

In this study, the imidazole-2-thione series was found to interact with metalloproteinases, and compound **24** exhibited measurable MMP-9 inhibition. However, the micromolar potency and moderate enzymatic inhibition relative to classical hydroxamate standards indicate that MMP-9 is likely a contributing, but not dominant, target. Instead, the overall biological activity of compound **24** reflects a broader polypharmacological mechanism involving interference with multiple cancer-relevant pathways. This includes MMP modulation, disruption of cell-cycle progression, accumulation of DNA damage, induction of apoptosis, and downregulation of metastasis-associated factors such as *MMP-9* and *hTERT*. The combined modulation of these pathways provides a compelling explanation for the compound's dual cytotoxic and anti-metastatic phenotype.

Such a dual-function profile could be particularly valuable in aggressive cancers—including triple-negative breast cancer, metastatic melanoma, or high-grade gliomas—where both cytotoxic debulking and control of invasive spread are critical. Future development should focus on structural optimisation to enhance potency and drug-like properties, detailed mechanism-of-action studies, and comprehensive *in vivo* evaluation in metastatic models. By moving beyond a single-target strategy (e.g. MMP inhibition alone) towards a broader phenotypic approach, this work demonstrates the potential of imidazole-2-thione derivatives as a novel class of anticancer therapeutics capable of addressing both tumour growth and metastasis—the deadliest trait of cancer.

Author contributions

CRediT: **Božena Golcienė**: Formal analysis, Methodology, Validation, Writing – review & editing; **Natalia Maciejewska**: Conceptualization, Formal analysis, Methodology, Validation, Visualization, Writing – original draft, Writing – review & editing; **Anoop Kallingal**: Formal analysis, Methodology, Writing – original draft; **Birutė Sapijanskaitė-Banevič**: Formal analysis, Methodology, Validation, Writing – review & editing; **Maryna Stasevych**: Formal analysis, Methodology, Writing – review & editing; **Vytautas Mickevičius**: Formal analysis, Methodology, Writing – original draft, Writing – review & editing.

Disclosure statement

The authors report no conflicts of interest.

Funding

This work is supported by Politechnika Gdańska (DEC–2/2021/IDUB/V0.6/Si).

ORCID

Natalia Maciejewska http://orcid.org/0000-0001-9942-285X
Birutė Sapijanskaitė-Banevič http://orcid.org/0000-0001-9090-9127
Maryna Stasevych http://orcid.org/0000-0001-5042-4133
Vytautas Mickevičius http://orcid.org/0000-0002-9961-2941

Data availability statement

Data will be made available on request.

References

1. Seyfried TN, Huysentruyt LC. On the origin of cancer metastasis. Crit Rev Oncog. 2013;18(1-2):43–73.
2. Nussinov R, Yavuz BR, Jang H. Molecular principles underlying aggressive cancers. Signal Transduct Target Ther. 2025;10(1):42.
3. Shi X, Wang X, Yao W, Shi D, Shao X, Lu Z, Chai Y, Song J, Tang W, Wang X, et al. Mechanism insights and therapeutic intervention of tumor metastasis: latest developments and perspectives. Signal Transduct Target Ther. 2024;9(1):192.
4. Esposito M, Ganesan S, Kang Y. Emerging strategies for treating metastasis. Nat Cancer. 2021;2(3):258–270.
5. Doostmohammadi A, Jooya H, Ghorbanian K, Gohari S, Dadashpour M. Potentials and future perspectives of multi-target drugs in cancer treatment: the next generation anti-cancer agents. Cell Commun Signal. 2024;22(1):228.
6. Bergonzini C, Kroese K, Zweemer AJM, Danen EHJ. Targeting integrins for cancer therapy: disappointments and opportunities. Front Cell Dev Biol. 2022;10:863850.
7. Liu J, Tsao MS, Pagura M, Shalinsky DR, Khoka R, Fata J, Johnston MR. Early combined treatment with carboplatin and the MMP inhibitor, prinomastat, prolongs survival and reduces systemic metastasis in an aggressive orthotopic lung cancer model. Lung Cancer. 2003;42(3):335–344.
8. Vermorken JB, Guigay J, Mesia R, Trigo JM, Keilholz U, Kerber A, Bethe U, Picard M, Brummendorf TH. Phase I/II trial of cilengitide with cetuximab, cisplatin and 5-fluorouracil in recurrent and/or metastatic squamous cell cancer of the head and neck: findings of the phase I part. Br J Cancer. 2011;104(11):1691–1696.
9. Bramhall SR, Hallissey MT, Whiting J, Scholefield J, Tierney G, Stuart RC, Hawkins RE, McCulloch P, Maughan T, Brown PD, et al. Marimastat as maintenance therapy for patients with advanced gastric cancer: a randomised trial. Br J Cancer. 2002;86(12):1864–1870.
10. Rulhania S, Kumar S, Nehra B, Gupta G, Monga V. An insight into the medicinal perspective of synthetic analogs of imidazole. J Mol Struct. 2021;1232:129982.
11. Verma A, Joshi S, Singh D. Imidazole: having versatile biological activities. J Chem. 2013;2013(1):329412.
12. Yadav G, Jain R. An insight into synthetic, structural and medicinal perspective of imidazole analogs: a review. Eur J Med Chem. 2025;290:117524.
13. Ortiz R, Perazzoli G, Cabeza L, Jiménez-Luna C, Luque R, Prados J, Melguizo C. Temozolomide: an updated overview of resistance mechanisms, nanotechnology advances and clinical applications. Curr Neuropharmacol. 2021;19(4):513–537.
14. Gao Y, Ding Y, Tai XR, Zhang C, Wang D. Ponatinib: an update on its drug targets, therapeutic potential and safety. Biochim Biophys Acta Rev Cancer. 2023;1878(5):188949.
15. Lalic H, Aurer I, Batinic D, Visnjic D, Smoljo T, Babic A. Bendamustine: a review of pharmacology, clinical use and immunological effects. Oncol Rep. 2022;47(6):114.
16. Maret W, Vallee BL. Thiolate ligands in metallothionein confer redox activity on zinc clusters. Proc Natl Acad Sci U S A. 1998;95(7):3478–3482.
17. Ramanathan RK, Kirkpatrick DL, Belani CP, Friedland D, Green SB, Chow H-HS, Cordova CA, Stratton SP, Sharlow ER, Baker A, et al. A phase I pharmacokinetic and pharmacodynamic study of PX-12, a novel inhibitor of thioredoxin-1, in patients with advanced solid tumors. Clin Cancer Res. 2007;13(7):2109–2114.
18. Ramanathan RK, Stephenson JJ, Weiss GJ, Pestano LA, Lowe A, Hiscox A, Leos RA, Martin JC, Kirkpatrick L, Richards DA, et al. A phase I trial of PX-12, a small-molecule inhibitor of thioredoxin-1, administered as a 72-hour infusion every 21 days in patients with advanced cancers refractory to standard therapy. Invest New Drugs. 2012;30(4):1591–1596.
19. Jordan BF, Runquist M, Raghunand N, Gillies RJ, Tate WR, Powis G, Baker AF. The thioredoxin-1 inhibitor 1-methylpropyl 2-imidazolyl disulfide (PX-12) decreases vascular permeability in tumor xenografts monitored by dynamic contrast enhanced magnetic resonance imaging. Clin Cancer Res. 2005;11(2 Pt 1):529–536.
20. Balandis B, Mickevičius V, Petrikaitė V. Exploration of benzenesulfonamide-bearing imidazole derivatives activity in triple-negative breast cancer and melanoma 2D and 3D cell cultures. Pharmaceuticals (Basel). 2021;14(11):1158.
21. Ozkay Y, Işikdağ I, Incesu Z, Akalin G. Synthesis of 2-substituted-N-[4-(1-methyl-4,5-diphenyl-1H-imidazole-2-yl)phenyl]acetamide derivatives and evaluation of their anticancer activity. Eur J Med Chem. 2010;45(8):3320–3328.
22. Yadav S, Lim SM, Ramasamy K, Vasudevan M, Shah SAA, Mathur A, Narasimhan B. Synthesis and evaluation of antimicrobial, antitubercular and anticancer activities of 2-(1-benzoyl-1H-benzo[d]imidazol-2-ylthio)-N-substituted acetamides. Chem Cent J. 2018;12(1):66.
23. Li N, Xu M, Zhang L, Lei Z, Chen C, Zhang T, Chen L, Sun J. Discovery of novel celastrol–imidazole derivatives with anticancer activity in vitro and in vivo. J Med Chem. 2022;65(6):4578–4589.
24. Golcienė B, Vaickelionienė R, Endriulaitytė U, Mickevičius V, Petrikaitė V. Synthesis and effect of 4-acetylphenylamine-based imidazole derivatives on migration and growth of 3D cultures of breast, prostate and brain cancer cells. Sci Rep. 2024;14(1):28065.
25. Pijuan J, Barceló C, Moreno DF, Maiques O, Sisó P, Marti RM, Macià A, Panosa A. In vitro cell migration, invasion, and adhesion assays: from cell imaging to data analysis. Front Cell Dev Biol. 2019;7:107.
26. Merlos Rodrigo MA, Casar B, Michalkova H, Jimenez Jimenez AM, Heger Z, Adam V. Extending the applicability of in ovo and ex ovo chicken chorioallantoic membrane assays to study cytostatic activity in neuroblastoma cells. Front Oncol. 2021;11:707366.

27. Ohno Y, Yi R, Suganami A, Tamura Y, Matsumoto A, Matsumoto S, Saito K, Shirasawa H. CCL299, a benzimidazole derivative induces G1 phase arrest and apoptosis in cancer cells. Anticancer Res. 2021;41(2):699–706.
28. Sherr CJ, Roberts JM. CDK inhibitors: positive and negative regulators of G1-phase progression. Genes Dev. 1999;13(12):1501–1512.
29. Engeland K. Cell cycle regulation: p53-p21-RB signaling. Cell Death Differ. 2022;29(5):946–960.
30. Pellegata NS, Antoniono RJ, Redpath JL, Stanbridge EJ. DNA damage and p53-mediated cell cycle arrest: a reevaluation. Proc Natl Acad Sci U S A. 1996;93(26):15209–15214.
31. Ling YH, el-Naggar AK, Priebe W, Perez-Soler R. Cell cycle-dependent cytotoxicity, G2/M phase arrest, and disruption of p34cdc2/cyclin B1 activity induced by doxorubicin in synchronized P388 cells. Mol Pharmacol. 1996;49(5):832–841.
32. Rello-Varona S, Gámez A, Moreno V, Stockert JC, Cristóbal J, Pacheco M, Cañete M, Juarranz A, Villanueva A. Metaphase arrest and cell death induced by etoposide on HeLa cells. Int J Biochem Cell Biol. 2006;38(12):2183–2195.
33. Pfeffer CM, Singh ATK. Apoptosis: a target for anticancer therapy. Int J Mol Sci. 2018;19(2):448.
34. Poon IKH, Lucas CD, Rossi AG, Ravichandran KS. Apoptotic cell clearance: basic biology and therapeutic potential. Nat Rev Immunol. 2014;14(3):166–180.
35. Chatelut E, Delord JP, Canal P. Toxicity patterns of cytotoxic drugs. Invest New Drugs. 2003;21(2):141–148.
36. Su J-X, Li S-J, Zhou X-F, Zhang Z-J, Yan Y, Liu S-L, Qi Q. Chemotherapy-induced metastasis: molecular mechanisms and clinical therapies. Acta Pharmacol Sin. 2023;44(9):1725–1736.
37. Zhao Y, He M, Cui L, Gao M, Zhang M, Yue F, Shi T, Yang X, Pan Y, Zheng X, et al. Chemotherapy exacerbates ovarian cancer cell migration and cancer stem cell-like characteristics through GLI1. Br J Cancer. 2020;122(11):1638–1648.
38. Škarková A, Bizzarri M, Janoštiak R, Mašek J, Rosel D, Brábek J. Educate, not kill: treating cancer without triggering its defenses. Trends Mol Med. 2024;30(7):673–685.
39. Pawlikowska P, Tayoun T, Oulhen M, Faugeroux V, Rouffiac V, Aberlenc A, Pommier AL, Honore A, Marty V, Bawa O, et al. Exploitation of the chick embryo chorioallantoic membrane (CAM) as a platform for anti-metastatic drug testing. Sci Rep. 2020;10(1):16876.
40. Rodrigues DB, Reis RL, Pirraco RP. Modelling the complex nature of the tumor microenvironment: 3D tumor spheroids as an evolving tool. J Biomed Sci. 2024;31(1):13.
41. Brüningk SC, Rivens I, Box C, Oelfke U, ter Haar G. 3D tumour spheroids for the prediction of the effects of radiation and hyperthermia treatments. Sci Rep. 2020;10(1):1653.
42. Chu PY, Koh APF, Antony J, Huang RYJ. Applications of the chick chorioallantoic membrane as an alternative model for cancer studies. Cells Tissues Organs. 2022;211(2):222–237.
43. Hincke MT, Da Silva M, Guyot N, Gautron J, McKee MD, Guabiraba-Brito R, Réhault-Godbert S. Dynamics of structural barriers and innate immune components during incubation of the avian egg: critical interplay between autonomous embryonic development and maternal anticipation. J Innate Immun. 2019;11(2):111–124.
44. Vandenbroucke RE, Libert C. Is there new hope for therapeutic matrix metalloproteinase inhibition? Nat Rev Drug Discov. 2014;13(12):904–927.
45. Shay JW, Wright WE. Telomerase: a target for cancer therapeutics. Cancer Cell. 2002;2(4):257–265.
46. Hannen R, Bartsch JW. Essential roles of telomerase reverse transcriptase hTERT in cancer stemness and metastasis. FEBS Lett. 2018;592(12):2023–2031.
47. Liu H, Liu Q, Ge Y, Zhao Q, Zheng X, Zhao Y. hTERT promotes cell adhesion and migration independent of telomerase activity. Sci Rep. 2016;6(1):22886.
48. Tang B, Xie R, Qin Y, Xiao Y-F, Yong X, Zheng L, Dong H, Yang S-M. Human telomerase reverse transcriptase (hTERT) promotes gastric cancer invasion through cooperating with c-Myc to upregulate heparanase expression. Oncotarget. 2016;7(10):11364–11379.
49. Liu M, Zhang Y, Jian Y, Gu L, Zhang D, Zhou H, Wang Y, Xu ZX. The regulations of telomerase reverse transcriptase (TERT) in cancer. Cell Death Dis. 2024;15(1):90. 26
50. Benhar M. Oxidants, antioxidants and thiol redox switches in the control of regulated cell death pathways. Antioxidants (Basel). 2020;9(4):309. 11
51. Grek CL, Townsend DM, Tew KD. The impact of redox and thiol status on the bone marrow: Pharmacological intervention strategies. Pharmacol Ther. 2011;129(2):172–184.
52. Shin HR, You BR, Park WH. PX-12-induced HeLa cell death is associated with oxidative stress and GSH depletion. Oncol Lett. 2013;6(6):1804–1810.
53. Volk-Draper L, Hall K, Griggs C, Rajput S, Kohio P, DeNardo D, Ran S. Paclitaxel therapy promotes breast cancer metastasis in a TLR4-dependent manner. Cancer Res. 2014;74(19):5421–5434.
54. Sun Z, Zhou D, Yang J, Zhang D. Doxorubicin promotes breast cancer cell migration and invasion via DCAF13. FEBS Open Bio. 2022;12(1):221–230.
55. Tolcher AW, Mayer LD. Improving combination cancer therapy: the CombiPlex® development platform. Future Oncol. 2018;14(13):1317–1332.